



UNF Digital Commons

UNF Graduate Theses and Dissertations

Student Scholarship

2012

Passive Gas-Liquid Separation Using Hydrophobic Porous Polymer Membranes: A Study on the Effect of Operating Pressure on Membrane Area Requirement

Taylor Patrick Maxwell
University of North Florida

Suggested Citation

Maxwell, Taylor Patrick, "Passive Gas-Liquid Separation Using Hydrophobic Porous Polymer Membranes: A Study on the Effect of Operating Pressure on Membrane Area Requirement" (2012). *UNF Graduate Theses and Dissertations*. 351.
<https://digitalcommons.unf.edu/etd/351>

This Master's Thesis is brought to you for free and open access by the Student Scholarship at UNF Digital Commons. It has been accepted for inclusion in UNF Graduate Theses and Dissertations by an authorized administrator of UNF Digital Commons. For more information, please contact [Digital Projects](#).

© 2012 All Rights Reserved



PASSIVE GAS-LIQUID SEPARATION USING HYDROPHOBIC
POROUS POLYMER MEMBRANES: A STUDY ON THE EFFECT OF
OPERATING PRESSURE ON MEMBRANE AREA REQUIREMENT

By

Taylor Patrick Maxwell

A thesis submitted to the School of Engineering
in partial fulfillment of the requirements for the degree of

Master of Science in Mechanical Engineering

UNIVERSITY OF NORTH FLORIDA

COLLEGE OF COMPUTING, ENGINEERING, AND CONSTRUCTION

August, 2012

Unpublished work © Taylor P. Maxwell

CERTIFICATE OF APPROVAL

The thesis of Taylor Patrick Maxwell is approved:

(Date)

Signature Deleted

8/6/12

Dr. James Fletcher

Signature Deleted

8/6/12

Dr. Richard V. Conte

Signature Deleted

8/2/2012

Dr. Adel El-Safty

Accepted for the Engineering Department:

Signature Deleted

8/7/2012

Dr. Murat Tiryakoglu

Accepted for the College of Computing, Engineering and Construction:

Signature Deleted

8/9/12

Dean Mark A. Tumeo

Accepted for the University:

Signature Deleted

8/27/12

Dr. Len Roberson

TABLE OF CONTENTS

	<u>page</u>
LIST OF TABLES	v
LIST OF FIGURES	vi
ABSTRACT.....	viii
Chapter 1	1
TOPIC INTRODUCTION.....	1
Chapter 2	4
LITERATURE REVIEW	4
Gas-Liquid Separation Models, Designs, and Performance	4
Two-Phase Flow	9
Characteristics of Gaseous Flow through Porous Media	10
Membrane Characterization.....	12
Chapter 3	15
MODEL DEVELOPMENT	15
Model Conditions and Assumptions	15
Bubble Venting Dynamics	16
Theoretical Active Membrane Length	19
Chapter 4	22
EXPERIMENTAL METHOD.....	22
Membrane Characterization.....	22
Liquid Entry Pressure (LEP).....	24
Active Membrane.....	26

Chapter 5.....	29
RESULTS AND DISCUSSION.....	29
Membrane Characterization.....	29
Liquid Entry Pressure (LEP).....	30
Active Membrane.....	32
FIGURES AND IMAGES.....	39
Theoretical Model with Repeated Experimental Data.....	39
Constant Gas Flow Curves.....	44
Constant Liquid Flow Curves.....	45
Two-Phase Flow Patterns.....	47
Chapter 6.....	48
CONCLUSION.....	48
REFERENCES.....	51
BIOGRAPHICAL SKETCH.....	53

LIST OF TABLES

Table 5-1: Summary of LEP data.	31
Table 5-2: Summary of “best fit” analysis for membrane reduction per unit channel pressure..	36

LIST OF FIGURES

Figure 1-1: Schematic of working principle of portable GLS.	2
Figure 3-1: Summary of simplified GLS model conditions.	16
Figure 3-2: Control volume analysis of gas bubble	17
Figure 4-1: SEM image of the EPTFE pore structure.....	23
Figure 4-2: Membrane characterization experimental setup.	23
Figure 4-3: Experimental setup for determining liquid entry pressure (LEP) of membrane.	25
Figure 4-4: 3-D model of GLS prototype components (flow channel block and cover plate). ...	26
Figure 4-5: Experimental setup for determining the active membrane length under various test conditions.....	27
Figure 5-1: Permeability plot for three separate membrane samples of the same type.	29
Figure 5-2: Overall permeability plot for the combined sample data.	30
Figure 5-3: Active membrane length data for 10mL/min liquid flow and 10sccm gas flow.....	39
Figure 5-4: Active membrane length data for 10mL/min liquid flow and 20sccm gas flow.....	39
Figure 5-5: Active membrane length data for 10mL/min liquid flow and 40sccm gas flow.....	40
Figure 5-6: Active membrane length data for 20mL/min liquid flow and 10sccm gas flow.....	40
Figure 5-7: Active membrane length data for 20mL/min liquid flow and 20sccm gas flow.....	41
Figure 5-8: Active membrane length data for 20mL/min and 40sccm gas flow.	41
Figure 5-9: Active membrane length for 40mL/min liquid flow and 10sccm gas flow.	42
Figure 5-10: Active membrane length for 40mL/min liquid flow and 20sccm gas flow.	42
Figure 5-11: Active membrane length for 40mL/min liquid flow and 40sccm gas flow.	43

Figure 5-12: Theoretical de-wetting velocity as a function of the static contact angle for water at 21°C.	43
Figure 5-13: Constant gas flow curves for 10mL/min liquid flow experiment.	44
Figure 5-14: Constant gas flow curves for 20mL/min liquid flow experiment.	44
Figure 5-15: Constant gas flow curves for 40mL/min liquid flow experiment.	45
Figure 5-16: Constant liquid flow curves for 10sccm gas flow experiment.	45
Figure 5-17: Constant liquid flow curves for 20sccm gas flow experiment.	46
Figure 5-18: Constant liquid flow curves for 40sccm gas flow experiment.	46
Figure 5-19: Liquid = 10mL/min, Gas = 40sccm.	46
Figure 5-20: Liquid = 20mL/min, Gas = 40sccm.	47
Figure 5-21: Liquid = 40mL/min, Gas = 10sccm.	46
Figure 5-22: Liquid = 40mL/min, Gas = 20sccm.	47
Figure 5-23: Liquid = 40mL/min, Gas = 40sccm	47

Abstract of Thesis Presented to the Graduate School
of the University of North Florida in Partial Fulfillment of the
Requirements for the Degree of Master of Science

PASSIVE GAS-LIQUID SEPARATION USING HYDROPHOBIC
POROUS POLYMER MEMBRANES: A STUDY ON THE EFFECT OF
OPERATING PRESSURE ON MEMBRANE AREA REQUIREMENT

By

Taylor Patrick Maxwell

July 2012

Chair: Dr. James Fletcher
Major: Mechanical Engineering

The use of hydrophobic porous polymer membranes to vent unwanted gas bubbles from liquid streams is becoming increasingly more common in portable applications such as direct methanol fuel cells (DMFCs) and micro-fluidic cooling of electronic circuits. In order for these portable systems to keep up with the ever increasing demand of the mobile user, it is essential that auxiliary components, like gas-liquid separators (GLS), continue to decrease in weight and size. While there has been significant progress made in the field of membrane-based gas-liquid separation, the ability to miniaturize such devices has not been thoroughly addressed in the available literature. Thus, it was the purpose of this work to shed light on the scope of GLS miniaturization by examining how the amount porous membrane required to completely separate gas bubbles from a liquid stream varies with operating pressure. Two membrane characterization experiments were also employed to determine the permeability, K_d , and liquid entry pressure (LEP) of the membrane, which provided satisfying results. These parameters

were then implemented into a mathematical model for predicting the theoretical membrane area required for a specified two-phase flow, and the results were compared to experimental values. It was shown that the drastically different surface properties of the wetted materials within the GLS device, namely polytetrafluoroethylene (PTFE) and acrylic, caused the actual membrane area requirement to be higher than the theoretical predictions by a constant amount. By analyzing the individual effects of gas and liquid flow, it was also shown that the membrane area requirement increased significantly when the liquid velocity exceeded an amount necessary to cause the flow regime to transition from wedging/slug flow to wavy/semi-annular flow.

CHAPTER 1

TOPIC INTRODUCTION

Gas-liquid separation devices (GLS) are used in many applications where the presence of gas bubbles within a liquid stream is considered undesirable. These devices can take on many different shapes and sizes, although they typically fall into one of two categories: 1) those that require power to remove the gas (active) and 2) those that do not require power (passive).

Usually, passive gas-liquid separation is the preferred technique since the device does not have a direct impact on the system efficiency; however, this method may be more readily applicable to certain situations than others. For instance, passive gas-liquid separation is relatively straightforward for stationary devices because the gas can be repeatedly vented in the upward direction by buoyancy driven forces, but when it comes to portable applications, the passive GLS approach becomes more complex. This is primarily because gas removal must occur at all orientations without losing any liquid, and the device volume must be as small as possible for packaging and maneuverability purposes.

One method of passive GLS design that has shown great promise for portable applications involves the use of a hydrophobic porous polymer membrane. Porous hydrophobic membranes, such as expanded polytetrafluoroethylene (EPTFE), are typically manufactured by stretching a solid sheet of the material until micrometer-sized voids develop within a sample. Due to the small pore sizes and hydrophobic properties achievable in such membranes, large capillary pressures are required to force liquid through the membrane, but gases are able to pass through with relative ease. As one can imagine, these characteristics are very desirable for

applications involving the separation of a two-phase fluid into its constituent phases, especially if the application is portable in nature. An example of a portable application that would benefit from the use of an EPTFE membrane to separate gas bubbles from a liquid stream is direct methanol fuel cells (DMFCs). The anode reaction in a DMFC is known to cause the production CO_2 gas within the liquid fuel stream, and if the gas is not vented, the system can experience a loss of efficiency due to blocked reaction sites and result in liquid leaks from over-pressurization. By utilizing a low depth flow channel design (as illustrated in Figure 1-1) with a hydrophobic porous polymer membrane in direct contact with the two-phase fluid stream, the idea of a passive-portable GLS becomes more feasible for an application like DMFCs.

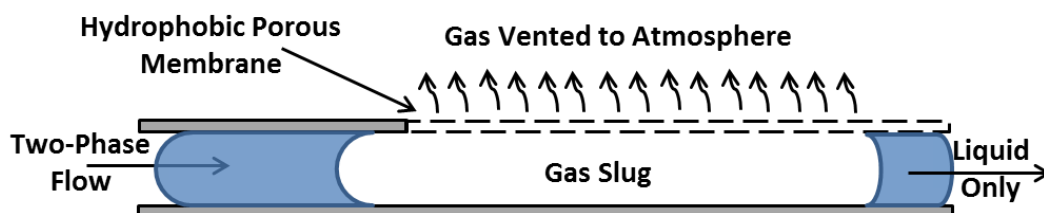


Figure 1-1: Schematic of working principle of portable GLS.

As the two-phase fluid enters the GLS device, the liquid is repelled by the hydrophobic membrane and retained within the flow channel, while the gas bubbles are forced through the membrane via pressure gradient. Since this method of gas-liquid separation is dictated by pressure driven forces, rather than buoyancy forces, it not only increases the viability for orientation independence, but also size miniaturization. The overall size of the GLS system is more easily minimized for this type of design because, less membrane area is required to vent a specified volume of gas at higher membrane pressure gradients. For instance, it has been observed that if the venting environment is at standard atmospheric conditions ($\sim 1\text{atm}$), then the minimum amount of active membrane area required to vent 100% of incoming gas bubbles can be significantly reduced by applying back pressure to the system. However, this approach to

GLS size miniaturization is not without its complications and limitations. The primary reasons for this are the following:

- Certain combinations of gas-liquid flow rates can result in undesirable two-phase flow structures that hinder gas venting.
- Temperature gradients can lead to condensation within the membrane pores which can also disrupt the gas venting process.
- Applying too much back pressure can cause large system pressure losses and membrane flooding.

The first two items imply that certain operating conditions may conflict with the potential benefits of applying back pressure to the GLS, while the third item indicates that there exists an upper limit as to how much back pressure can be applied before system performance becomes compromised. Furthermore, since the GLS literature currently available provide very little theoretical or experimental data on how the active membrane area responds to incremental changes in system pressure; this work will focus on taking the first step in analyzing the problem. That is, a fundamental analysis on the reduction of active membrane area as a function of channel pressure (i.e. applied back pressure) will be conducted for a single membrane type and GLS orientation, and for a variety of different two-phase flow rates. The effect of temperature and orientation will be left to future research.

The analysis for this work will include the following:

- The use of various membrane characterization techniques to extract key parameters for modeling the gas venting process.
- A mathematical model for predicting the amount of active membrane required to separate a specified two-phase flow as a function of gas type, membrane permeability, channel geometry, average channel pressure, and initial bubble velocity.
- The results of several active membrane experiments will be presented and discussed to illustrate the validity of the model as well as offer guidance for future GLS designs.

CHAPTER 2 LITERATURE REVIEW

Gas-Liquid Separation Models, Designs, and Performance

In order to gain an understanding of the current state of GLS research, several published models, designs, and performance data were reviewed. The focus of this review was limited to gas-liquid separation for applications involving bubbly two-phase flow through similar sized micro channels. The gas-liquid separation techniques consisted of those that utilized precision drilled micro holes (i.e membrane-less), although the focus was primarily aimed at those that used porous membranes (i.e membrane-based) to vent the gas, since porous membranes are commercially available.

Membrane-Less Methods

Chuang, et al. [1], have successfully developed a passive waste-management device (PWMD) with the capability to vent CO₂ generated by a micro direct methanol fuel cell, while simultaneously transporting water and methanol residue to a reservoir for reuse. The design utilized concepts such as condensation, temperature gradient, surface tension gradient, and droplet coalescence to meet the requirements. In order to test the performance of the device the authors conducted various experiments to measure the device's ability to retain unused liquid fuel and to exhaust the CO₂ from the device. They reported that the device was able to remove excess liquid at a reasonable rate and that all CO₂ bubbles were vented with the assistance of buoyancy forces and successive gas bubbles.

Meng et al. [2] investigated two types of GLS methods, membrane-less and membrane-based. The two different devices were described as “bubble-sink devices” that used surface energy minimization to capture and vent carbon dioxide bubbles. Both types of bubble sinks consisted of a small chamber where carbon dioxide bubbles were generated via chemical reaction, however, the two types of degassing plates used to vent CO₂ manifested very different results. The first generation degassing plate consisted of a polypropylene plate with Teflon coated vent holes (~50 µm in diameter) surrounded by a hydrophilic (SiO₂) matrix. This design aimed to attract the bubbles to the hydrophobic surface by promoting the formation of the solid-vapor interface, thus decreasing the overall surface energy of the system. By using a CCD camera the authors found that the relatively large venting holes allowed for fast venting (~20 seconds) but also led to liquid intrusion into the pores.

Membrane-Based Methods

The second generation prototype developed by Meng, et al., employed the use of a hydrophobic porous membrane with an average pore size of ~0.2 µm. The membrane was sandwiched between two silicon chips with a square array of KOH-etched pits (~200µm). The pits were intended to lower the overall surface energy of the system by increasing the bubble contact area with the surface and reduce the liquid-vapor interface of the bubble. For similar test conditions as the first generation, the authors reported that the second generation prototype provided better bubble capture performance while also withstanding liquid leaks at a higher pressure (~38 psi).

In another membrane based design, Zhu [3] explored two different gas-liquid separation concepts (cross flow and dead head configuration) which utilized both hydrophilic and hydrophobic membranes. The two configurations were tested solely on their ability to separate

the gas and liquid components of the flow. It was reported that at the design pressure conditions (i.e. 10psi) the dead head configuration achieved complete gas-liquid separation, whereas the cross flow configuration did not. On the other hand, it the cross flow design was able to filter water at a higher flow rate (6 $\mu\text{l}/\text{min}/\text{psi}$) than the dead head design (2.2 $\mu\text{l}/\text{min}/\text{psi}$). These two phenomena were attributed to the lower flow resistance in the micro channel of the cross flow configuration; thus, resulting in more water segments able to flow through micro channel or the hydrophilic membrane per unit time [3].

Authors Meng and Kim [4] proposed and tested a method of pumping and recirculating liquid fuel in a micro direct methanol fuel cell (μDMFC) by utilizing momentum of the CO_2 gas bubbles generated in the anode before they were expelled through a micro porous membrane. In order to validate the theory of operation the authors conducted an experiment in which they initially operated a fuel cell with an external pump. Once the fuel cell began producing power the external pump was removed from the circuit and the system was allowed to operate on the proposed self-circulating bubble driven mechanism. The fuel circulation mechanism was deemed successful by displaying continuous operation of the fuel cell for over 70 minutes.

Kraus and Krewer [5] also demonstrated a membrane-based gas-liquid separation device for micro direct methanol fuel cells and experimentally evaluated its performance at various orientations and operating conditions. The device consisted of a jig made of PMMA with milled flow channels (1.7 μm wide by 500 μm deep) and a hydrophobic PTFE membrane cover. They determined that at design conditions (i.e. $V_{\text{liquid}} = 0.916 \text{ mL} \cdot \text{min}^{-1}$, $V_{\text{gas}} = 10 \text{ NmL} \cdot \text{min}^{-1}$, $T_{\text{env}} = 20^\circ\text{C}$, $T_{\text{sys}} = 60^\circ\text{C}$, $\text{RH}_{\text{env}} = 80\%$, $P_{\text{sys}} = 3\text{kPa}$), 100% of the supplied CO_2 gas was separated at all orientations 90° from the “normal” configuration. However, it was also determined that as the liquid volume flow rate increased, the maximum allowable flow rate of CO_2 (to ensure 100% gas

separation) decreased significantly. It was concluded that the liquid flow rate limits the minimum membrane area required to separate 100% of the gas supply from the liquid stream.

In another study conducted by Meng et al. [6], a one-dimensional venting rate model for the removal of CO₂ gas bubbles from the anodic channel of a micro direct methanol fuel cell (μ DMFC) was developed. Two prototypes were constructed with two different hydrophobic nanoporous membranes (PTFE and polypropylene) on top of a square cross-sectional micro channel. To test the validity of the theoretical model, venting rates were measured for pure water and a 10 molar methanol mixture, and limited to two pressure settings (0.8 and 0.5 psi) for each fluid. Though all the CO₂ bubbles were successfully removed in each experiment, the measured venting rate tended to be slower than that predicted by the theoretical model. This result was attributed to the presence of liquid within the micro channel, which was not accounted for in the theoretical model. It was then concluded that the venting rate was limited by how quickly the liquid could be displaced from an active venting area (i.e. de-wetting velocity), thereby allowing gas to access a dry membrane surface.

In a manner similar to the previously reviewed work [6], Xu et al. [7] also modeled the bubble venting rate of CO₂ through a microporous membrane; however, the authors of this work proposed a set of design criteria that must be met to ensure the complete separation of gas from liquid. In general, the author's data for bubble extraction time as a function of bubble length was in good agreement with the corresponding theoretical predictions for the membrane with 0.2 μ m pore size. However, for the remaining membranes with pore sizes of 1.2 and 10 μ m, the data was much more scattered. The scattering behavior was attributed to the bubble velocity exceeding the critical (de-wetting) velocity, thus causing the formation of a stable liquid film between the gas bubbles and the membrane surface.

Another application where microporous membranes have been used to vent unwanted gas bubbles is in the microfluidic cooling of electronic circuits. David et al. [8] visually analyzed the bubble venting process for both adiabatic and diabatic two-phase flow, in a single copper micro channel with a hydrophobic porous membrane wall. With the use of a high speed camera and an ex-situ test device, the authors were able to characterize how the mass quality (i.e. ratio of air flow to total flow) influenced the venting effectiveness (i.e. venting rate per unit pressure, kg/s/Pa) for the three different liquid Weber numbers. It was found that as mass quality increased for each Weber number there was initially a linear increase in venting effectiveness followed by a maximum peak.

For the highest Weber number it was observed that the formation of long annular air structures at mass qualities greater than 1% impeded the air from contacting the membrane until much further downstream, thus resulting in a much smaller venting area seen by the air slugs before reaching the channel outlet [8]. The flow structures of the two lower Weber number experiments were determined to resemble bubbly/wavy type flows which allowed for more immediate air-membrane contact, and therefore, a higher venting effectiveness.

Fang et al. [9] attempted to model the gas-liquid separation process by creating 3D numerical simulations based on the volume of fluid (VOF) method. This method was used to visualize the venting process of a vapor bubble through porous membrane wall. During the vapor venting simulation the authors were able to analyze the velocity field within a single bubble as well as the surrounding area, and determined that as the bubble contacted the membrane surface the vapor flow initially experienced a high resistance. This resistance caused the vapor bubble to expand over the membrane surface, reach a maximum venting rate, followed

by the subsequent shrinking and disappearance of the bubble [9]. It was then concluded that the simulation results were comparable to that provided by David et al. [8].

Two-Phase Flow

Another important aspect of gas/liquid separation is the flow characteristics associated with the incoming two-phase fluid. Depending on the relative flow rates of the gas and liquid phases the gas bubble distribution can result in many different forms. Cubaud and Ho [10] investigated two-phase flow in square micro-channels (200 and 525 μm) by focusing on five main flow regimes: 1) bubbly, 2) wedging, 3) slug, 4) annular, and 5) dry flow. The authors determined that the transition between each flow regime occurred at predictable ratios of liquid flow to total flow for channel heights less than 1mm. Similar results were reported by Zhao et al. [11], although, Zhao et al. found that for channel heights less than 0.3mm the transition between flow regimes occurred at smaller gas flow rates and bubbly flow was never observed.

Wilmarth et al. [12] also studied two-phase flow in rectangular channels, but for 1mm and 2mm channel heights at vertical and horizontal orientations. It was determined that the flow regimes for the different dimensioned channels were similar for a constant orientation. However, the flow regimes that were observed for vertical flow were different from those observed for horizontal flow for the same flow channel dimensions.

Taitel and Dukler [13] attempted to develop a theoretical model for predicting the flow regime transitions in horizontal two-phase flow. The model was made up of five dimensionless equations to predict the transition boundaries between flow regimes as a function of pipe size, fluid properties, and angle of inclination. Based on the model a two-dimensional flow map was developed and used to study the effect of operating variables on regime boundaries. By using a

specific mapping method it was determined that the regime boundaries were relatively insensitive to pipe size (2-30cm diameter) for two-phase flows at low pressures (~1 atm). However, the regime boundaries were found to shift significantly for two-phase systems at higher pressures (~68 atm) and slight inclinations.

Characteristics of Gaseous Flow through Porous Media

Though there have been other approaches to modeling gas transport through porous media (i.e. Solution diffusion model [14]), the most general and widely accepted model is the ‘Dusty gas’ model (DGM), developed by Mason [15]. Mason proposed that the general form of the ‘Dusty gas’ model, for gas transport through porous media, can be described by a combination of three flow mechanisms:

1. Viscous flow, which is associated with total pressure gradients and limited by the membrane geometry and viscosity of the gas.
2. Molecular diffusion, dependent on concentration gradient and diffusivity.
3. Knudsen diffusion, where the flow of gas is dominated by molecule-wall collisions.

The DGM model characterized the porous membrane as uniformly, distributed dust particles held stationary in space. This approach allowed Mason to derive the DGM model from kinetic gas theory, making it more theoretically sound than the other empirical models [15]. The DGM, as derived by Mason, was represented by the following two equations:

$$\frac{N_i^D}{D_{ie}^k} + \sum_{j=1 \neq i}^n \frac{P_j N_i^D - P_i N_j^D}{D_{ije}^0} = \frac{-1}{RT} \nabla P_i \quad \text{Eq. 2-1}$$

$$N_i^V = \frac{-P_i B_o}{RT\mu} \nabla P \quad \text{Eq. 2-2}$$

where Eq. 2-1 represents the total diffusive flux (N_i^D) of component i, Eq. 2-2 represents the viscous flux (N_i^V) of component i, P is the total pressure, P_i is the partial pressure of component i, and μ is the fluid viscosity. The viscous flow parameter, B_o , and diffusivities $D_{i\ j e}^0$ (molecular) and $D_{i e}^k$ (Knudsen) are experimental constants that depend on the gas type, membrane geometry, and operating conditions. It was also noted that for the special case of one dimensional, pure viscous flow through porous media, the steady state volumetric gas flux can be reduced from the general form of Eq. 2-2 to Darcy's law:

$$V'' = \frac{K_d \Delta P}{\mu \delta_t} \quad \text{Eq. 2-3}$$

where, μ is the gas viscosity, δ_t is the membrane thickness, and ΔP is the pressure difference across the membrane. The term, K_d , is the bulk membrane permeability coefficient and is typically represented by the following relation:

$$K_d = \frac{\varepsilon D_{pore}^2}{32\tau} \quad \text{Eq. 2-4}$$

where ε is the membrane porosity, D_{pore} is the diameter of a single pore, and τ is the membrane tortuosity.

The DGM model was further developed in a collaborative work by Mason and Malinaukas [16], where special cases involving uniform pressure and temperature were used to simplify the general form of the DGM. Lawson et al.[17] also addressed some simplifications of the DGM in their work involving membrane distillation models; and showed that certain flow mechanisms may be considered negligible in comparison to others if the interaction between the membrane and molecules were more favorable for a particular mechanism. Overall, Lawson et al. found that the 'Dusty gas' model was a reliable method for modeling gas flow through porous media; however, since the general model is only valid for isothermal flux it was recommended

that thermal diffusion and thermal transpiration terms should be included in the model to reduce error [17].

Membrane Characterization

When determining which type of membrane is more appropriate for a specific application, accurate knowledge of structural properties and their characteristics are often limited by the information provided by membrane manufacturers. To satisfy this need for reliable membrane properties numerous experimental techniques have been developed over the years. However, researchers often stress that the characterization method chosen should reflect the level of detail and accuracy required by the application, and be such that the medium of the characterization and final application are similar [18].

For applications where detailed information of the pore size distribution was required (i.e. food, pharmaceutical, electronics, etc.), Martinez et al. [18] and Shao et al. [19] achieved satisfactory results using variations of the gas-liquid displacement method. In general, the process consists of flooding the membrane pores by using a pressurized wetting liquid. Then, an inert displacement gas (typically Nitrogen) is used to force the wetting liquid through the membrane until no liquid remains within the pores. As the liquid is forced out of the membrane, flux measurements of the displacement gas are measured as a function of the membrane pressure gradient. With this information the experimenter can evaluate a distribution of pore sizes for membranes with very complex geometries.

For applications where detailed knowledge of the pore size distribution is not required Mason and Malinaukas [16] proposed a method for extracting other structural properties from a microporous membrane using data obtained from single gas experiments. In general, the method

utilizes lumped permeability factors obtained from flow versus pressure data that can be used to approximate the average pore size, porosity, and/or tortuosity. The implementation of this model was demonstrated by Yashuda et al. [20] in their work on estimating the average pore size of porous polymer membranes from gas permeability data.

In order to estimate the pore size of a particular membrane Yashuda et al. began by acquiring flux versus pressure drop data for a variety of membranes with nominal pore sizes ranging between 0.025-0.10 μm . Since membranes with sub-micron pore sizes are known to be associated with flow in the Knudsen-viscous transition regime the following expression for permeability, K , was used:

$$K = K_o + \left(\frac{B_o}{\eta}\right) \Delta \bar{P} \quad \text{Eq. 2-5}$$

Where K_o was the Knudsen permeability coefficient, η was the gas viscosity, B_o was the viscous parameter, and $\Delta \bar{P}$ was the mean membrane pressure. By plotting the permeability, K , versus the mean pressure the authors were able to obtain K_o and B_o by extrapolating the data to the point of zero pressure and by determining the slope of the plot, respectively. By using the expressions for K_o , B_o , and mean molecular velocity (proposed by Mason et al. [15]), Yashuda et al. derived the following relation for predicting the mean pore size, m :

$$m = \left(\frac{B_o}{K_o}\right) \left(\frac{16}{3}\right) \left(\frac{2RT}{\pi}\right)^{1/2} M^{-1/2} \quad \text{Eq. 2-6}$$

Where R is the universal gas constant, T is the absolute gas temperature, and M is the average molecular weight. Based on their results, it was concluded that the proposed method predicted pore size values consistent with nominal values for a variety of membranes and gases.

Guijt et al. [21] also used a single gas technique (similar to the one previously described) in their work on modeling membrane distillation modules. However, in this work the authors investigated the effect of gas species on the permeability coefficients, K_o and B_o . They found that for a given membrane the values of K_o and B_o obtained using Nitrogen and carbon dioxide were within each other's margin of error. When using Helium, however, all of the K_o values were slightly less and all of the B_o values were greater than those obtained using N_2 and CO_2 . The authors attributed this behavior to the heterogeneous nature of the membranes, but the primary cause of the error was believed to be a result of the large mean molecular speed associated with the low molecular weight of Helium [21].

CHAPTER 3 MODEL DEVELOPMENT

Model Conditions and Assumptions

When studying the effect of back pressure on the required amount of GLS active membrane it is useful to develop a theoretical model that can serve as a reference for the experimental results. However, in complex systems it is often difficult to distinguish the relationship between two specific variables. Therefore, the following assumptions were made in an effort to minimize any extraneous effects that might obscure the direct relationship between the back pressure and active membrane.

- 1.) Surfactants and temperature gradients can lead to venting failures by either membrane “wetting” or blockage caused by capillary condensation [22, 23]. In order to avoid these effects, the model was limited to the separation of CO₂ gas from deionized water at room temperature (~21°C).
- 2.) All diffusion effects were considered negligible in comparison to the viscous flow:
 - a. *Molecular diffusion* was considered negligible because the concentration gradient of CO₂ exiting through the membrane is on the same order of magnitude as the concentration gradient of air entering through the membrane; and as a result, the net molecular diffusion out of the membrane is negligibly small compared to the pressure driven flow (i.e. viscous flow).
 - b. *Knudsen diffusion* was assumed to be negligible for all conditions of interest because, it is only significant when the mean free path of the diffusing gas is greater than or equal to the pore size of the membrane. This is a valid assumption because the pore size is at least one order of magnitude greater than the mean free path of CO₂ for all conditions of interest.
- 3.) The surrounding venting environment is assumed to be at typical laboratory conditions (i.e. T~21°C, P~1atm, R.H.~65%).

4.) The GLS is constrained by the following assumptions (summarized in Figure 3-1):

- a. The flow channel has a straight, constant rectangular cross-section, where one wall is replaced with a hydrophobic porous polymer membrane ($\sim 1 \mu\text{m}$ pore size, $\sim 100 \mu\text{m}$ thickness).
- b. The model is only valid for GLS orientations for which the flow direction is parallel to the horizontal plane.
- c. The axial pressure drop along flow channel is assumed to be small in comparison to the membrane pressure drop and linear along the channel length.
- d. The pressure everywhere within the GLS is assumed to be well below the liquid entry pressure (LEP) of the membrane (discussed in more detail later).
- e. The incoming two-phase flow is assumed to be steady and in the wedging/slug flow regime, such that the gas bubbles expand over the entire channel cross section and are unaffected by the surrounding liquid.

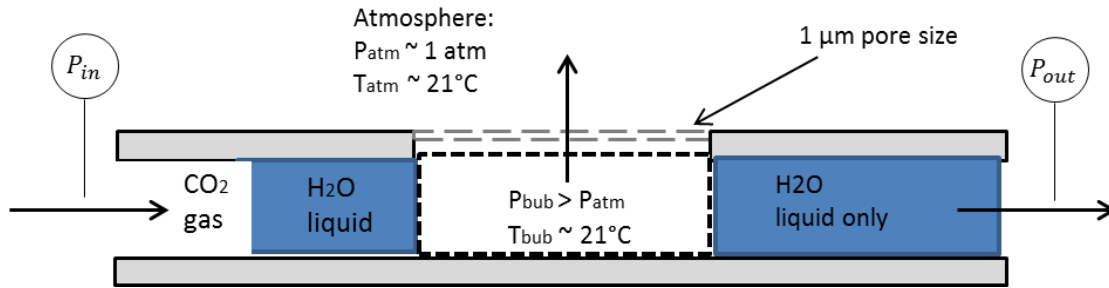


Figure 3-1: Summary of simplified GLS model conditions.

Bubble Venting Dynamics

In order to develop an expression that relates the active membrane area to the applied back pressure it is necessary to analyze the process by which a single gas bubble is separated from the GLS flow channel. Based on the conditions summarized in Figure 3-1, the dynamics of a gas bubble moving along a porous surface in the x-direction can be represented as a moving/deforming control volume, as seen in Figure 3-2.

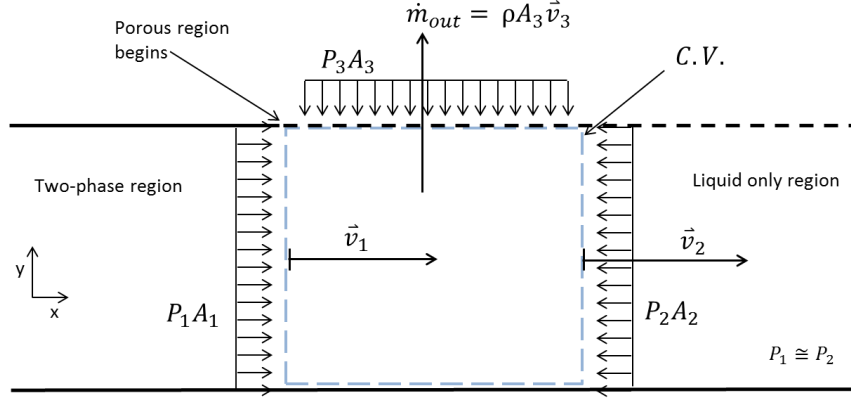


Figure 3-2: Control volume analysis of gas bubble

By examining the control volume in Figure 3-2, the integrated form of the mass continuity equation can be expressed as:

$$\frac{dm_{cv}}{dt} = -\dot{m}_{out} \quad \text{Eq. 3-1}$$

Assuming that the gas bubble flows through the membrane via Darcy flow, such that the bubble is incompressible in the porous region of the GLS and shrinks only in the x-direction, then Eq.

3-1 can be written in terms of the relative velocities, \vec{v}_1 , \vec{v}_2 , and \vec{v}_3 :

$$A_2\vec{v}_2 - A_1\vec{v}_1 = -A_3\vec{v}_3 \quad \text{Eq. 3-2}$$

$$A_{bub,cs}(\vec{v}_1 - \vec{v}_2) = A_{bub,i}\vec{v}_3 \quad \text{Eq. 3-3}$$

where, $A_{bub,cs}$ is the cross sectional area of the bubble within the channel, $A_{bub,i}$ is the initial gas bubble area in contact with porous membrane (not to be confused with the active membrane area). Also, since the width of the bubble, w_{bub} , and the height of the bubble, h_{bub} , are assumed to be equivalent to their respective channel dimensions (assumption 4e), then Eq. 3-3 reduces to:

$$h_{chan}(\vec{v}_1 - \vec{v}_2) = l_{bub,i}v_{mem} \quad \text{Eq. 3-4}$$

Where velocities \vec{v}_1 , \vec{v}_2 , and \vec{v}_{mem} are the average velocities at the bubble rear, bubble front, and membrane wall, respectively; and $l_{bub,i}$ is the initial bubble length.

Furthermore, since the gas flow through the membrane is dictated by the total pressure gradient across the membrane (assumption 2), the average membrane wall velocity, \vec{v}_{mem} , can be estimated from (Eq. 2-5), which is the Darcy form of the Dusty gas model for viscous flow through porous media. It should also be noted that the volumetric wall flux is equivalent to the average membrane wall velocity, $V'' = \dot{V}/A_{mem} = \vec{v}_{mem}$:

$$\vec{v}_{mem} = \frac{K_d}{\mu\delta_t} \Delta P_{mem} = \frac{K_d}{\mu\delta_t} (P_{bub} - P_{atm}) \quad \text{Eq. 3-5}$$

where K_d is the membrane permeability (determined experimentally), μ is the viscosity of the gas bubble, δ_t is the average membrane thickness, and P_{bub} is the pressure within the bubble. Due to the inherent difficulties of measuring the pressure within a gas bubble, it is assumed that the bubble pressure, P_{bub} , can be approximated as the average pressure within the GLS flow channel, $P_{chan,avg} = \frac{P_{in}+P_{out}}{2}$; as long as the pressure drop across the flow channel is small and linear with respect to the channel length (assumption 4c).

Combining the expressions in Eq. 3-4 and Eq. 3-5, and solving for the bubble front velocity, \vec{v}_2 , gives:

$$\vec{v}_2 = \vec{v}_1 - \frac{l_{bub,i}}{h_{chan}} \left[\frac{K_d}{\mu\delta_t} (P_{chan,avg} - P_{atm}) \right] \quad \text{Eq. 3-6}$$

If the bubble rear velocity, \vec{v}_1 , is assumed to be constant and equal to the superficial bubble velocity of the incoming two-phase stream (in the non-porous region of the channel), then Eq. 3-6 provides a means of determining the bubble front velocity, \vec{v}_2 , as a function of the average channel pressure (i.e. applied back pressure) and the initial bubble length, $l_{bub,i}$. The superficial bubble velocity can be approximated as the sum of the individual gas and liquid velocities of the incoming two-phase stream (i.e. $\vec{v}_1 = \vec{v}_{liq} + \vec{v}_{gas}$), as long as the channel area is constant, the gas bubbles expand over the entire channel area, and the two-phases are immiscible. Based on

these conditions, any increase in gas or liquid flow will result in a proportional increase in bubble velocity (i.e. \vec{v}_1). Once the relative velocities \vec{v}_1 and \vec{v}_2 are known, the theoretical active membrane length can be approximated by the relations derived in the following section.

Theoretical Active Membrane Length

Based on the assumptions made heretofore, the minimum length of porous membrane required to completely vent a single gas bubble of initial length, $l_{bub,i}$, is dependent upon the relative bubble front and rear velocities, \vec{v}_2 and \vec{v}_1 , respectively. This relationship can be represented by the following kinematic equation:

$$l_{mem,act} = l_{bub,i} + \vec{v}_2 \Delta t \quad \text{Eq. 3-7}$$

where $l_{mem,act}$ is the theoretical active membrane length and $\Delta t = l_{bub,i}/(\vec{v}_1 - \vec{v}_2)$ represents the time required for the bubble rear to reach the bubble front. By substituting the expression for Δt and \vec{v}_2 , Eq. 3-7 becomes:

$$l_{mem,act} = l_{bub,i} \left(1 + \frac{\vec{v}_2}{\vec{v}_1 - \vec{v}_2} \right) \quad \text{Eq. 3-8}$$

$$l_{mem,act} = l_{bub,i} \left(\frac{\vec{v}_1}{\vec{v}_1 - \vec{v}_2} \right) \quad \text{Eq. 3-9}$$

$$l_{mem,act} = l_{bub,i} \left\{ \frac{\vec{v}_1}{\vec{v}_1 - \left[\vec{v}_1 - \frac{l_{bub,i}}{h_{chan}} \frac{K_d}{\mu \delta_t} (P_{chan,avg} - P_{atm}) \right]} \right\} \quad \text{Eq. 3-10}$$

By cancelling terms and rearranging, the final form of the active membrane length is given as:

$$l_{mem,act} = \frac{\mu \delta_t h_{chan}}{K_d} \frac{\vec{v}_1}{(P_{chan,avg} - P_{atm})} \quad \text{Eq. 3-11}$$

Eq. 3-11 provides a means of calculating the theoretical active membrane length, $l_{mem,act}$, with knowledge of the gas type, membrane permeability and thickness, channel geometry, bubble

velocity of the incoming two-phase flow, \vec{v}_1 , and average pressure within the flow channel, $P_{chan,avg}$. The theoretical model, which was initially derived from a per gas bubble analysis, can now be applied to a continuous two-phase flow, provided assumption 4 holds true. This approach allows for a much easier comparison between the experimental results and the theoretical predictions; since individual bubble length measurements are no longer required.

The relation in Eq. 3-11 is mathematically valid for all average channel pressures, with the exception of $P_{chan,avg} = P_{atm}$, which results in an undefined solution. However, for the purpose of this work, both the upstream pressure, P_1 , and the downstream pressure, P_2 , should be greater than the atmospheric pressure, so that the direction of gas flow is always towards the atmosphere. Furthermore, the pressure everywhere in the channel must be less than the liquid entry pressure (LEP) of the membrane pores, so as to not obstruct the gas vent path with liquid. This property can be measured experimentally (discussed more in Chapter 4) and/or approximated by the Laplace-Young equation [24]:

$$LEP = \frac{-2B\gamma_L \cos \theta}{r_{max}} \quad \text{Eq. 3-12}$$

where γ_L is the liquid surface tension, θ is the static liquid-membrane contact angle, r_{max} is the largest pore radius, and B is a geometric factor determined by the membrane structure (Note that $B = 1$ corresponds to a cylindrical pore structure).

The active membrane length relation (Eq. 3-11) is also valid for $\vec{v}_1 > \vec{v}_{liq}$, where the inequality is a reminder that there must be gas supplied to the liquid stream for it to be removed from the GLS (i.e. $\vec{v}_{gas} > 0$). However, the expression, $\vec{v}_1 > \vec{v}_{liq}$, does not completely describe the flow conditions for which the model is valid because it makes intuitive sense that the GLS will fail to remove 100% of the supplied gas at some sufficiently high channel velocity (i.e. as

$\vec{v}_1 \rightarrow \infty$). This limitation is described by the dynamic de-wetting velocity proposed by De Gennes [25]:

$$v_d = \frac{1}{12\sqrt{2}} \frac{\gamma/\mu}{a} \theta^3 \quad \text{Eq. 3-13}$$

where a is a dimensionless coefficient (approximately equal to 20), γ is the surface tension, μ is the viscosity, and θ is the static liquid-membrane contact angle. This quantity represents the bubble velocity limit, beyond which a liquid film can develop between the gas structure and dry membrane surface, and hence, impeded the gas venting process.

CHAPTER 4

EXPERIMENTAL METHOD

As the purpose of this work is to show how the application of back pressure can significantly reduce the active membrane length, the following experiments are required:

- 1.) A membrane characterization experiment is required to obtain the permeability coefficient, K_d , of the membrane type to be used in active membrane experiments. Once this parameter is obtained, it can be applied to the theoretical model (Eq. 3-11) to allow direct comparison between theoretical and experimental values of active membrane length under various flow and pressure conditions.
- 2.) A liquid entry pressure (LEP) experiment is necessary to determine how much back pressure can be applied before the capillary forces exceed the surface tension forces of the liquid-pore interface, thus resulting in membrane flooding. This information can then be used to ensure that all active membrane experiments are conducted within an appropriate range of pressures.
- 3.) A series of GLS experiments, involving a prototype similar to that depicted in Figure 1-1, are required to show how the active membrane length is affected by incremental changes in back pressure for various gas-liquid flow combinations and orientations.

Membrane Characterization

The type of expanded polytetrafluoroethylene (EPTFE) membrane used throughout this work was known to have an average pore diameter of $\sim 1\mu\text{m}$ and an average thickness of $\sim 100\mu\text{m}$. Since the manufacturing processes associated with these types of membranes often induce a wide distribution of pore sizes (as seen in Figure 4-1), it is more practical to obtain a bulk permeability coefficient of the membrane experimentally.

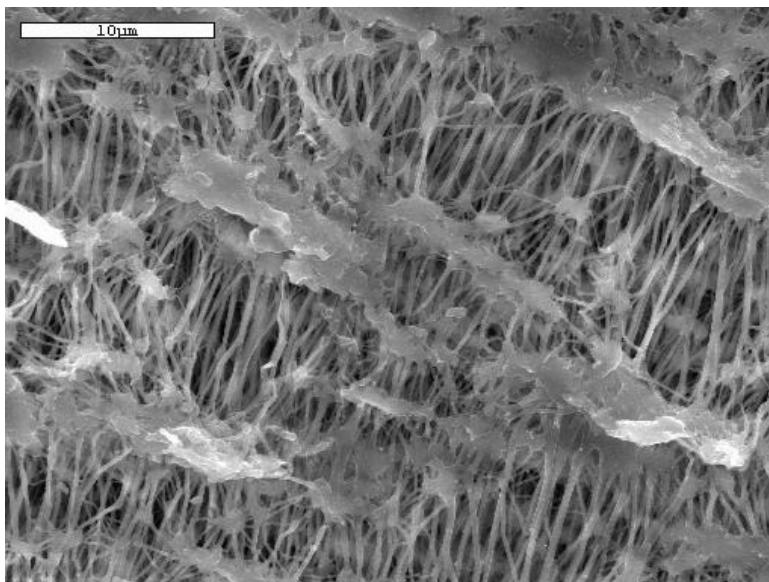


Figure 4-1: SEM image of the EPTFE pore structure.

In order to obtain the permeability coefficient, K_d , of the membrane, an air-tight test cell was used to secure a single flat-sheet membrane sample in an orientation perpendicular to the direction of gas flow. The pressure drop across the membrane sample was determined by measuring the pressure upstream of the test cell with a precision manometer and the downstream pressure was known to be atmospheric. A schematic of the experimental setup up is illustrated in Figure 4-2.

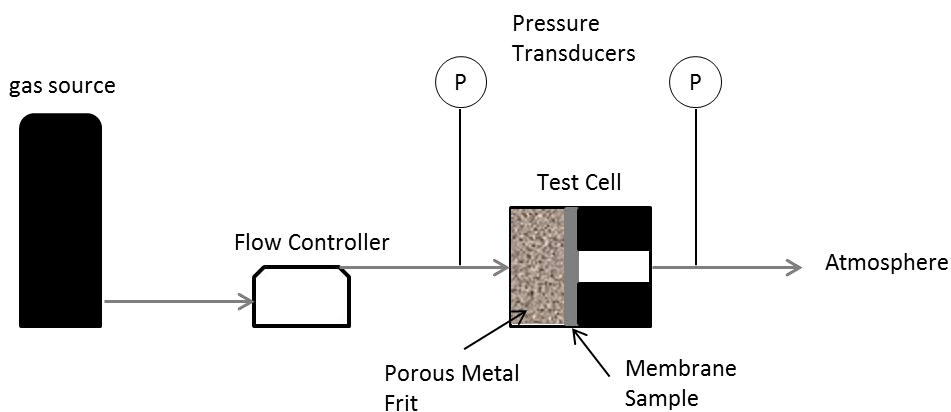


Figure 4-2: Membrane characterization experimental setup.

The test cell also possessed a porous metal frit in direct contact with the upstream side of the membrane, which was intended to give the sample structural support and evenly distribute the

gas over the sample, thus creating a uniform pressure drop over the sample area. For this particular work, carbon dioxide gas (CO_2) was used and the volumetric flow rate was varied between 20 and 300sccm using a mass flow controller. Once the membrane pressure drop was measured with respect to the corresponding flow rate, the permeability coefficient, K_d , was approximated by utilizing Eq. 2-5. For a constant gas viscosity and membrane thickness, pure viscous flux is known to increase linearly with respect to pressure gradient. Therefore, the average permeability, K_d , was determined from the slope of V'' versus $\Delta P_{mem}/(\mu\delta_t)$.

In an effort to reduce the amount of error associated with the calculated membrane permeability some additional factors were considered. For instance, the pressure drop across the test cell was measured without a membrane sample to determine its influence on the membrane pressure measurements. Also, since the membrane manufacturing process is not always consistent, several membrane samples were characterized and their thickness measured to ensure that the permeability and thickness values were repeatable.

Liquid Entry Pressure (LEP)

After the gas permeability of the membrane was obtained, the same test cell was used to determine the liquid pressure required to force liquid into the membrane pores (LEP). This was accomplished by securing a membrane sample in the test cell and filling the upstream portion of the test cell cavity with deionized water, such that the water level was visible in the feed line. The downstream side of the membrane and test cell cavity were maintained at atmospheric pressure and initially dry. Once the initial position of the liquid level was marked, a displacement gas (Nitrogen) was used to apply pressure to the system until the liquid penetrated through the membrane. However, since the downstream side of the membrane was not visible

within the test cell, the LEP was determined by monitoring the liquid level position in the feed line over time and noting the regulator pressure. An illustration of the experimental setup can be seen in Figure 4-3.

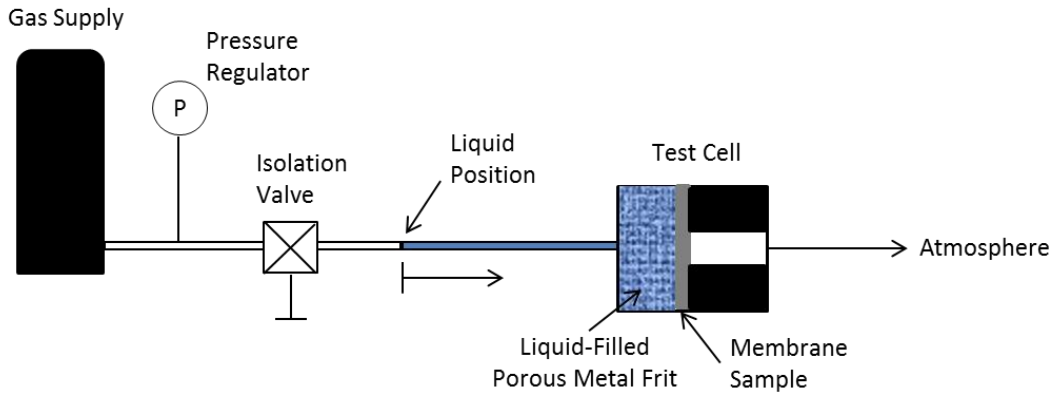


Figure 4-3: Experimental setup for determining liquid entry pressure (LEP) of membrane.

The liquid pressure was increased by 1psig increments with approximately 10 minutes between successive pressure increments to allow adequate time for the liquid to infiltrate the membrane pores. The LEP was approximated as the gas regulator pressure necessary to cause a continuous liquid level displacement over a 10 minute time interval. In order to reduce any hydrostatic pressure effects caused by liquid phase, the experimental test rig was maintained in the horizontal plane. Also, multiple membrane samples were tested to verify that the LEP of the membrane type was repeatable.

Once the experimental LEP values were obtained they were compared to the theoretical values predicted by the Laplace-Young equation (Eq. 3-12). The theoretical LEP values were based on the static contact angle (measured by the sessile drop method and Image-J software to $\pm 10^\circ$) and the nominal pore size values provided by the manufacturer. The surface tension of water was assumed to be 0.0726 N/m at 21°C and the pores were assumed to be cylindrical, such that the geometric factor, $B = 1$.

Active Membrane

In order to determine how the active membrane is influenced by the back pressure, it was first necessary to construct a simple GLS prototype device. The prototype consisted of two primary components: 1.) a flow channel block and 2.) a cover plate (as seen in Figure 4-4), between which a porous membrane sample was placed.

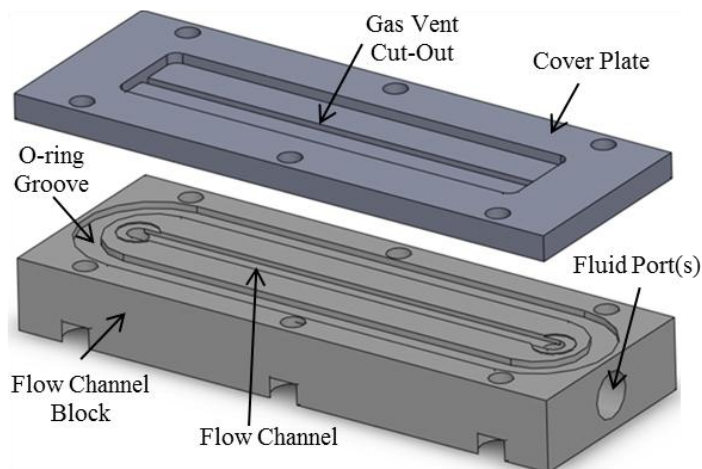


Figure 4-4: 3-D model of GLS prototype components (flow channel block and cover plate).

The block was made of transparent acrylic and had a single straight, open rectangular flow channel (0.870 mm deep, 4 mm wide, and 40 mm long). Two pressure taps were located on the back side of the flow channel block and were separated by a distance of 40mm (not illustrated in Figure 4-4). The cover plate had a 4mm wide by 40mm long cut-out to allow a clear path for the gas to vent to atmosphere. Once the GLS prototype was assembled and leak tested, a test setup was developed to allow the experimenter to visually observe the effect of applied back pressure on the active membrane length. The experimental setup is illustrated in Figure 4-5.

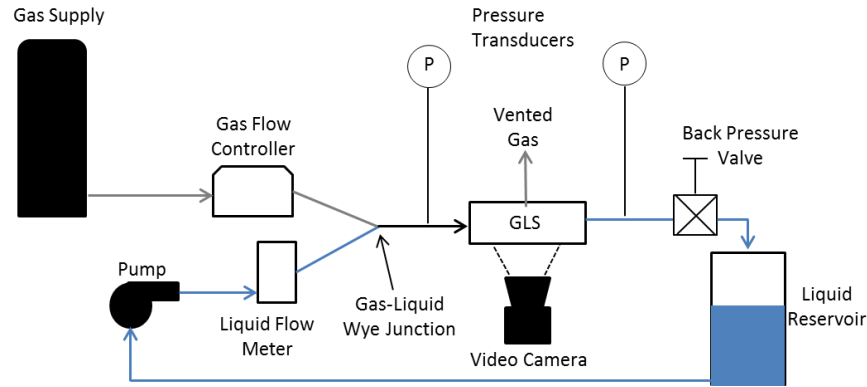


Figure 4-5: Experimental setup for determining the active membrane length under various test conditions.

The liquid flow was controlled by varying the voltage supplied to a positive displacement pump until the liquid flow meter indicated the desired flow set point, and the gas flow was set by a digital flow controller. The two fluids (CO_2 gas and de-ionized liquid water) were combined at a wye-junction, where a steady two-phase stream was created and routed to the GLS inlet port. By using a digital video camera, it was possible to record the active membrane behavior at different back pressure settings. The back pressure was varied by adjusting the position of a needle valve, located downstream of the GLS. The recorded videos were then analyzed using an image process software (Image-J) to determine the maximum distance the gas structures traveled before being vented through the membrane. Two pressure transducers (0-40in. H_2O range) were positioned at the flow channel inlet and exit, so that the average channel pressure could be determined without obstructing the view of the GLS flow channel.

For this series of experiments, the active membrane behavior was observed for various two-phase flow combinations involving volumetric liquid water flow rates of 10, 20, and 40 mL/min and CO_2 gas flow rates of 10, 20, and 40sccm. The GLS remained stationary during all testing and was positioned with the flow traveling parallel to the horizontal plane and the membrane facing downward to eliminate the possibility of buoyancy effects. The back pressure was adjusted such that the average channel pressure was well below the LEP of the membrane

and within the range of the upstream and downstream pressure transducers (0-40in. H₂O). All tests were performed at least two times to ensure that the results were repeatable.

CHAPTER 5 RESULTS AND DISCUSSION

Membrane Characterization

The membrane characterization data for three different samples of the same membrane type can be seen in Figure 5-1, along with the corresponding permeability coefficient, K_d , of each sample. As mentioned previously, it was important that the test cell (used to secure the membrane sample) did not significantly affect the membrane pressure drop measurements. For all conditions of interest, it was determined that test cell pressure drop never exceeded 5% of the combined membrane-test cell pressure drop. As a result, it was assumed that the membrane pressure drop, ΔP_{mem} , could be approximated as the combined membrane-test cell pressure drop without inducing significant error into the permeability calculations.

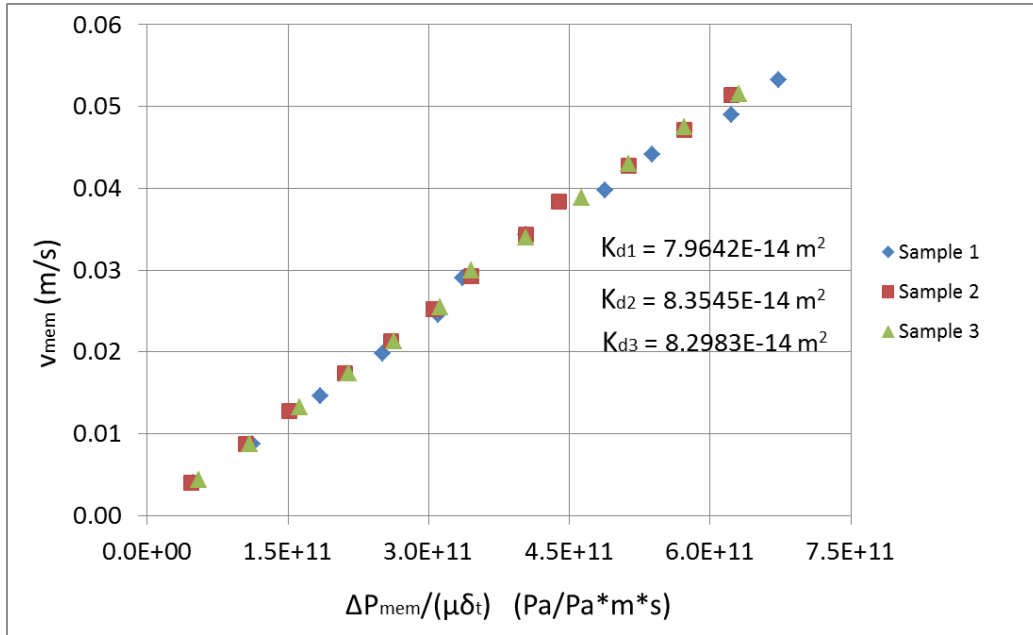


Figure 5-1: Permeability plot for three separate membrane samples of the same type.

As expected from Eq. 2-3, the general trend of the membrane wall velocity, v_{mem} , was determined to be linear with respect to $\Delta P_{mem}/(\mu\delta_t)$ for laminar flow through porous media. In fact, the coefficient of determination, R^2 , which represents the goodness of fit of the linear “best fit” model, was greater than 0.99 for each sample. It was also apparent that the permeability, K_d , of each sample was essentially the same value. Therefore, the permeability data for each sample was combined (as seen in Figure 5-2) to obtain an overall permeability, which was employed in the active membrane calculations (discussed later). The overall permeability coefficient was also found to be in good agreement with other similar works, such as the results of Guijt, et al. [21].

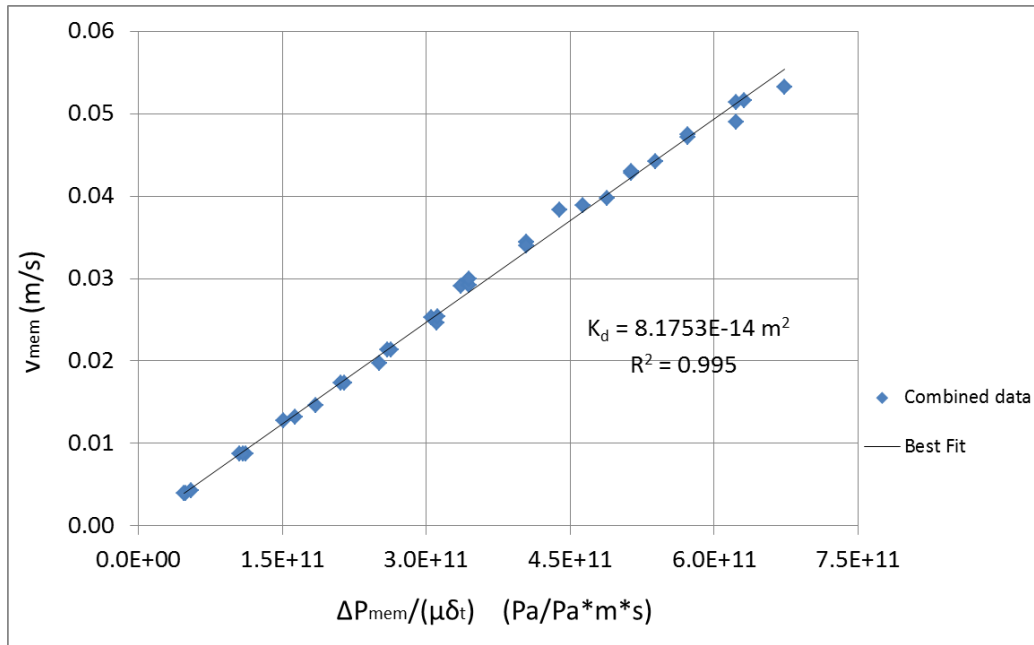


Figure 5-2: Overall permeability plot for the combined sample data.

Liquid Entry Pressure (LEP)

The data for all liquid entry pressure experiments are located in Table 5-1. Overall, the experimental LEP values were repeatable from sample to sample; however, the experimental values were also consistently lower than the theoretical values predicted by the Laplace-Young relation (Eq. 3-12). As it turned out, the magnitude of this discrepancy was not particularly

concerning for this work. Nevertheless, a brief discussion on the likely causes of these discrepancies and why the discrepancies were tolerated is detailed in the remainder of this section.

Sample #	Contact Angle (Deg)	Theoretical LEP (psig)	Experimental LEP Range (psig)	Percent Difference Range
1	125	24.1	15-15.5	55.5-60.66
2	128	25.9	15-15.5	67.1-72.6
3	123	22.9	14.5-15	52.6-58.0
Average	125.3	24.3	15.1	NA

Table 5-1: Summary of LEP data.

The possible causes for the discrepancy between the experimental and theoretical LEP values were attributed to the following:

- 1.) The membrane pores may have experienced stretching at sufficiently high liquid pressures, resulting in a larger average pore size than the expected nominal value; and hence, small experimental LEP values relative to theoretical values.
- 2.) An overestimation of the theoretical LEP may have been the result of an overestimation of the static contact.
- 3.) If the membrane has a wide pore size distribution, use of the average (nominal) pore radius in the theoretical LEP calculations may have induced significant error.

Since the membrane sample area used throughout the experiment was small ($\sim 1\text{cm}^2$) and the test cell was designed to provide additional structural support for the sample; the degree of membrane deflection allowed within the test cell was considered negligible. Based on these factors and the repeatable nature of the experiments, it appeared unlikely that the discrepancies were caused by any significant flaws associated with the direct LEP experiments, such as membrane pore stretching (item 1).

The measured/nominal quantities associated with the theoretical LEP calculations (i.e. items 2 and 3), on the other hand, were much more likely to be the source of the discrepancy. For instance, the contact angle measurement technique used in the current work was relatively

crude (accurate to $\pm 10^\circ$) compared other methods, which require more sophisticated equipment. This approach may have led to a repeated overestimation of the contact angle, and hence, an overestimation of the theoretical LEP. However, the primary reason for the discrepancy was likely the result of approximating the theoretical LEP with the average (nominal) pore radius instead of the maximum pore radius, as required by Eq. 3-12. This rather oversimplified approach was taken because the average pore radius was readily available, and its intended use was only to acquire a rough approximation of the LEP. Fortunately, the exact cause of the difference between theoretical and experimental LEP values was irrelevant because the maximum liquid pressure experienced by the membrane during the active membrane experiments (discussed in the following section) was significantly lower than the both the average theoretical and experimental LEPs. In fact, the liquid pressure never exceeded ~ 8 psig for all active membrane experiments.

Active Membrane

Located at the end of the chapter are the data plots for each individual active membrane experiment (Figure 5-3 through Figure 5-11). The data show how the active membrane length, $L_{mem,act}$, behaved as a function of the average channel pressure, $P_{chan,avg}$, for various combinations of two-phase flow using CO_2 gas and deionized liquid water. As mentioned earlier, it was important that the channel pressure drop remained as small as possible to ensure a constant membrane wall velocity, v_{mem} . By using error bars to denote the channel pressure drop experienced by each two-phase flow, it was possible to determine the validity of using the average channel pressure, $P_{chan,avg}$, to approximate the membrane wall velocity, v_{mem} , and hence, the active membrane length, $L_{mem,act}$. For the majority of flow conditions considered,

the channel pressure drop was determined to have an insignificant effect on the active membrane data ($\Delta P_{chan} < 1.11 \text{ in. } H_2O$). However, for the two-phase flow experiments containing 40mL/min of liquid water, the channel pressure drop was much greater ($2.1 < \Delta P_{chan} < 3.20 \text{ in. } H_2O$). Even though the channel pressure drop for the 40mL/min liquid flow experiments was greater than the 10 and 20mL/min liquid flow experiments, the results were tolerated for the following reasons: 1) the data was consistent between trials, 2) the results shared similar trends with the theoretical predictions, and 3) the portion of the error responsible for the discrepancy between the theoretical and experimental results was insignificant compared to other sources of error (discussed in more detail in the following section).

Model Evaluation and Effect of De-wetting Velocity

In general, the active membrane length for both the theoretical model and experimental data was initially quite high, and then experienced a significant reduction with increasing channel pressure. As the channel pressure continued to increase, the active membrane lengths asymptotically approached unique minimum values, which tended to increase with increasing two-phase flow. Even though the experimental curves possessed a hyperbolic-like shape very similar to the theoretical curves, it was clear that theoretical model had a stronger dependency on pressure. As a result of this stronger pressure dependence, the model consistently under predicted the active membrane length achievable for each experiment, resulting in a constant offset between the two curves. This discrepancy was attributed to the drastically different wetting characteristics of the EPTFE membrane and acrylic surfaces in contact with the gas-liquid flow. The next few paragraphs are devoted to explaining the nature of this discrepancy in more detail.

As mentioned in the theoretical modeling section, the separation of a flowing two-phase fluid (wedging/slug flow) into its constituent phases was assumed to be unimpeded by the liquid phase as long as the bubble velocity did not exceed the de-wetting velocity. The de-wetting velocity, which represents how quickly a liquid film can be displaced from a particular surface, was approximated from Eq. 3-13 and compared to the superficial bubble velocities of each active membrane experiment. Based on the measured liquid-membrane contact angle ($\sim 125^\circ$), the de-wetting velocity was calculated to be approximately six times greater than the highest expected bubble velocity for the series of experiments. This outcome would normally indicate that the de-wetting velocity was high enough to have a negligible impact on the gas venting process for all experiments. However, the use of the liquid-membrane contact angle to describe the de-wetting velocity for the overall GLS system was believed not to be valid for this case, since the liquid within the GLS channel was also in simultaneous contact with the relatively non-hydrophobic channel walls (i.e. acrylic). By measuring the contact angle of the channel material to be approximately 50° , it was determined that the liquid-channel de-wetting velocity was on the same order as the smallest expected bubble velocity for the active membrane experiments, and hence, non-negligible.

Based on these findings, it was believed that the local de-wetting velocity at the channel corners (i.e. where the EPTFE membrane and acrylic channel walls meet) was small enough to cause a momentary/partial liquid barrier between the gas structure and dry membrane surface. With the gas unable to achieve immediate access to all of the available membrane area, the bubbles were required to travel further downstream until enough liquid was displaced to allow complete venting to occur. As a result, the active membrane length curves were consistently shifted above the theoretical curves.

This de-wetting explanation could also lead one to expect the experimental curves to shift downward and approach the theoretical curves, if the channel walls were to be replaced with a more hydrophobic material. However, due to the cubic nature of the relationship between the contact angle and the de-wetting velocity (seen in Eq. 3-13), the contact angle must be increased by a non-negligible amount before all of the bubble velocities are well below the de-wetting limit. For example, Figure 5-12 shows that by increasing the contact angle from 50° to 60° the de-wetting velocity only increases from ~ 0.15 to ~ 0.25 m/s, which still leaves 5 of the 9 experiments prone to de-wetting interference. In order for the channel material to have sufficient hydrophobicity for purpose of this work, the contact angle should be at least 75° (assuming the measurement error to be $\pm 10^\circ$).

Another interesting observation to be noted from Figure 5-3 through Figure 5-11 was that as the total two-phase flow rate increased, the slope of the experimental curves also tended to become more linear, resulting in a growing deviation from the theoretical curves. This behavior was consistent with the proposed de-wetting explanation to a certain extent, since the constant nature of the de-wetting velocity was expected to cause more interference of the liquid phase as the bubble velocity increases with each experiment. However, due to the odd nature of the curves and significance of the deviation between the data and model, it was necessary to study the phenomenon more closely. The following sections discuss how the individual effects of the gas and liquid flow influenced the data.

Effect of Gas Flow on Active Membrane Length

The constant gas flow curves for active membrane length versus average channel pressure are depicted in Figure 5-13 through Figure 5-15. From these figures, the rate at which the active membrane length decreased with increasing channel pressure appeared to become

smaller as the gas flow set point increased. In other words, the ability to minimize the active membrane length by applying back pressure to the GLS was less effective at the higher gas flow conditions. In order to quantify these results and compare them to the theoretical values, the equation for the “best fit” of each experimental curve was determined, and used to calculate the slope. The “best fit” type was chosen based on how well it physically resembled the data, while maintaining a high coefficient of determination, R^2 . Table 5-2 summarizes the values for the rate of reduction of the active membrane length for both the experimental data and theoretical model.

Liquid Flow (mL/min)	Gas Flow (sccm)	Best Fit Equation Type	Coefficient of Determination, R^2	(Actual) Membrane Length Reduced Per Unit Channel Pressure (mm/in.H₂O)	(Theoretical) Membrane Length Reduced Per Unit Channel Pressure (mm/in.H₂O)	Percent Difference
10	10	4th order	0.9996	4.79	8.93	46.36
	20	4th order	0.9973	3.80	5.97	36.32
	40	3rd order	0.9956	2.88	3.58	19.47
20	10	Hyperbolic	0.989	3.85	5.97	35.44
	20	Hyperbolic	0.9908	3.09	4.47	30.82
	40	Hyperbolic	0.9958	2.02	2.98	32.34
40	10	Hyperbolic	0.9934	1.77	3.58	50.60
	20	4th order	0.9985	1.54	2.98	48.21
	40	3rd order	0.9989	1.28	2.24	42.58

Table 5-2: Summary of “best fit” analysis for membrane reduction per unit channel pressure.

As confirmed in Table 5-2, the rate of reduction of the active membrane length clearly decreased as the gas flow set point increased (i.e the slope achieved smaller negative values). In fact, the slopes of each gas curve appeared to decrease by an amount that was consistent with the direction of increasing gas flow. For example, for the 10mL/min liquid flow experiment, the slope was found to decrease by ~20.7% from 10 to 20sccm and by 24.2% from 20 to 40sccm. Similar results were also observed for the different gas flow settings of the 20 and 40mL/min

liquid flow experiments. While the magnitude of these percent increases were not exactly proportional to increase in gas flow, the general behavior made sense because the theoretical active membrane length (Eq. 3-11) was known to increase with two-phase (bubble) velocity, \vec{v}_1 , which increases with volumetric flow rate for a constant channel area.

Based on the curve fit analysis, it was believed that the gas flow was not the primary cause for the growing discrepancy at the higher two-phase flow conditions because the experimental data and theoretical model shared similar trends with respect to gas flow, and the percent error between the experimental and theoretical slopes tended to decrease with increasing gas flow. This claim was also supported by the fact that the percent error between calculated slope of the experimental gas curves and the theoretical model was noticeably larger (on average) for the 40mL/min liquid flow conditions.

Effect of Liquid Flow on Active Membrane Length

The constant liquid flow curves for active membrane length versus average channel pressure can be seen in Figure 5-16 through Figure 5-18. By representing the data in this manner, one can clearly see that the relationship between the active membrane length and the average channel pressure was more sensitive to the liquid velocity than the gas velocity; a result similar to the work of Kraus and Krewer [5]. For instance, the 40mL/min liquid flow curves clearly decreased at a slower rate with respect to the channel pressure than the 10 and 20mL/min liquid flow curves for all gas flow settings. Even though the error associated with the greater channel pressure drop compounded this discrepancy, its effect was insignificant by comparison and the uncharacteristic nature of the curve's slope indicated that some type of event was occurring between the 20 and 40mL/min liquid flow conditions, causing the gas venting process

to be hindered. In order to determine the source of this phenomenon, several snapshot images of the two-phase active membrane experiments were analyzed.

By observing and comparing the images in Figure 5-19 through Figure 5-23, it was apparent that the 40mL/min liquid flow experiments possessed a different two-phase flow pattern than the 10 and 20mL/min liquid flow experiments. The 40mL/min liquid flow experiment exhibited a wavy/semi-annular type structure, while the all of the 10 and 20mL/min liquid flow experiments maintained wedging/slug-like structures. These observations were similar to the higher liquid Weber number experiments conducted by David et al. [8], which suggested that the gas bubble was not in direct contact with porous membrane 100% of the time when such flow patterns existed. Based on these findings, it was inferred that the interference of the de-wetting velocity was particularly unfavorable for gas venting when the liquid channel velocity exceeds an amount (~ 0.1 - 0.2 m/s) necessary to cause a transition from wedging/slug flow to wavy/semi-annular flow. Since the two-phase structure was not in the fully annular regime, the active membrane length was still able to be reduced to its minimum value without exceeding the LEP of the membrane; however, a relatively greater channel pressure was required to do so.

FIGURES AND IMAGES

Theoretical Model with Repeated Experimental Data

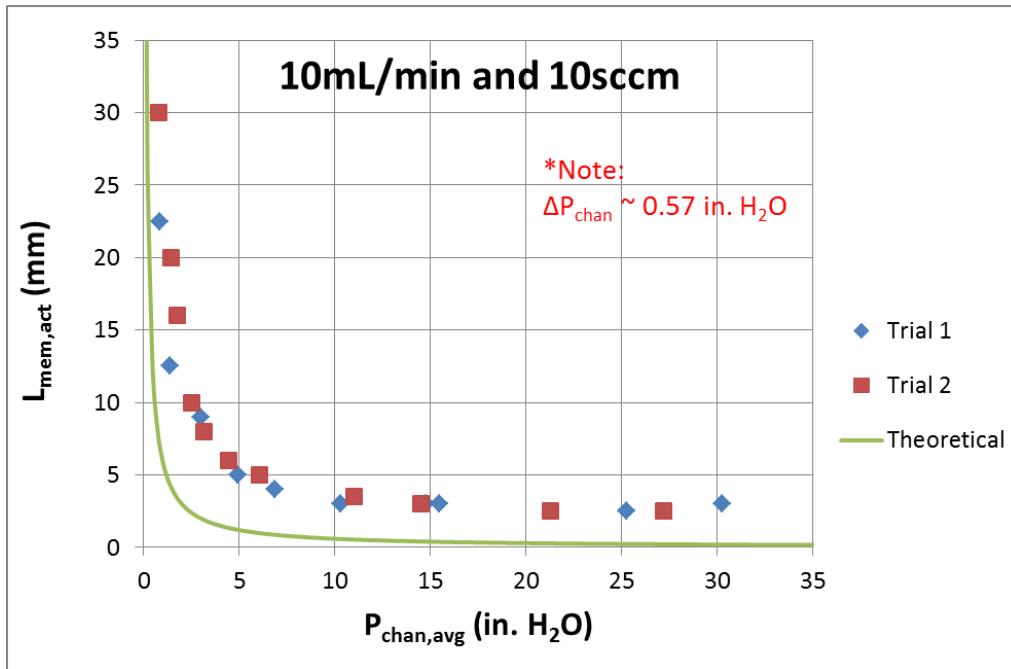


Figure 5-3: Active membrane length data for 10mL/min liquid flow and 10sccm gas flow.

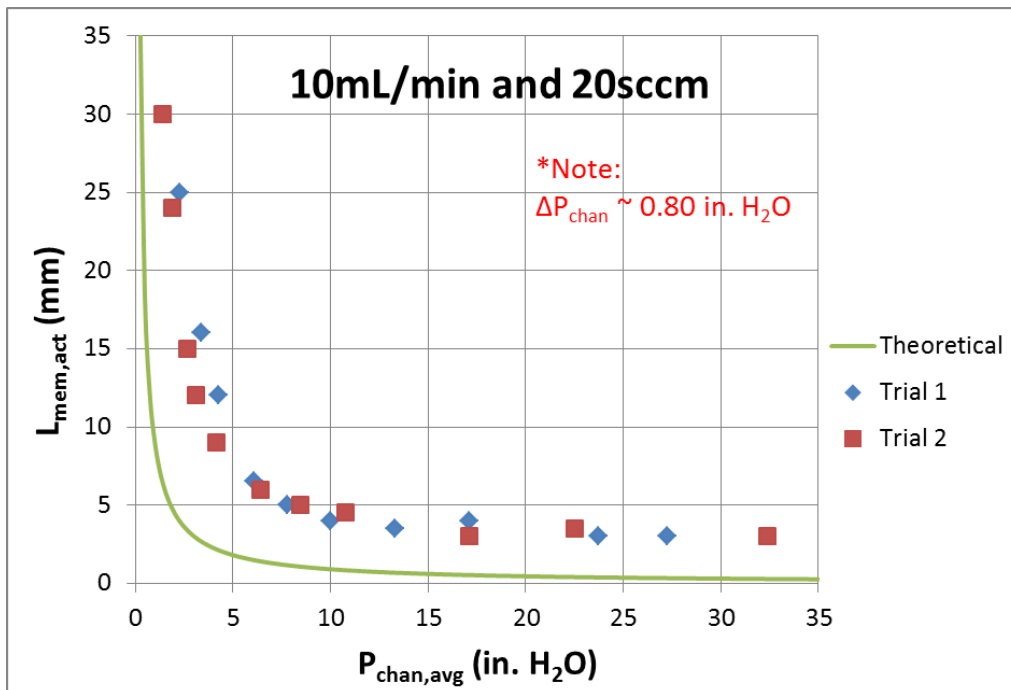


Figure 5-4: Active membrane length data for 10mL/min liquid flow and 20sccm gas flow.

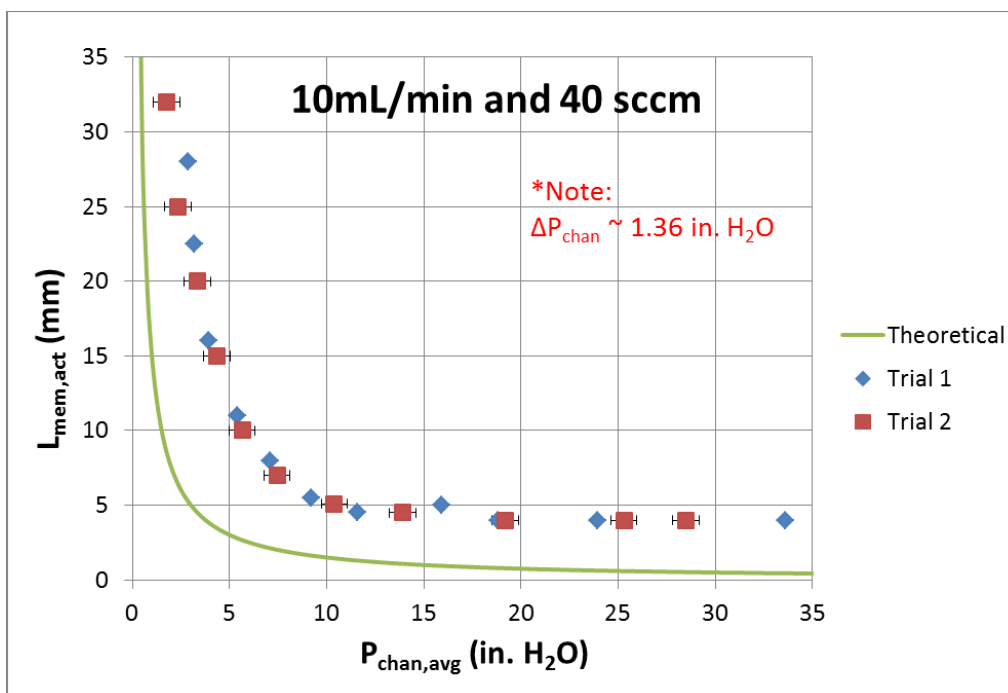


Figure 5-5: Active membrane length data for 10mL/min liquid flow and 40sccm gas flow.

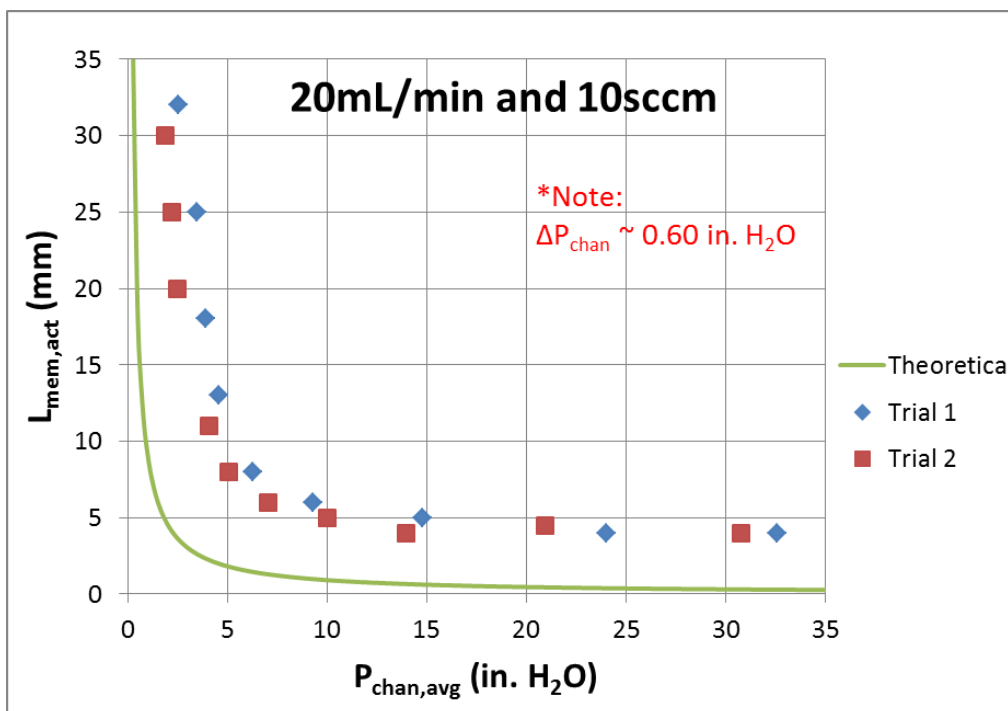


Figure 5-6: Active membrane length data for 20mL/min liquid flow and 10sccm gas flow.

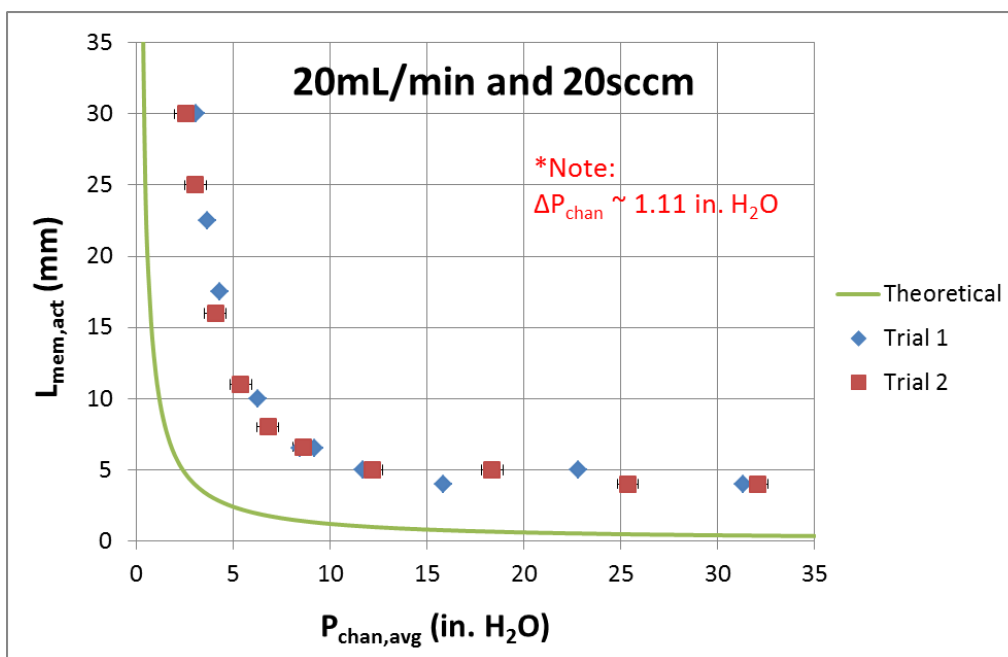


Figure 5-7: Active membrane length data for 20mL/min liquid flow and 20sccm gas flow.

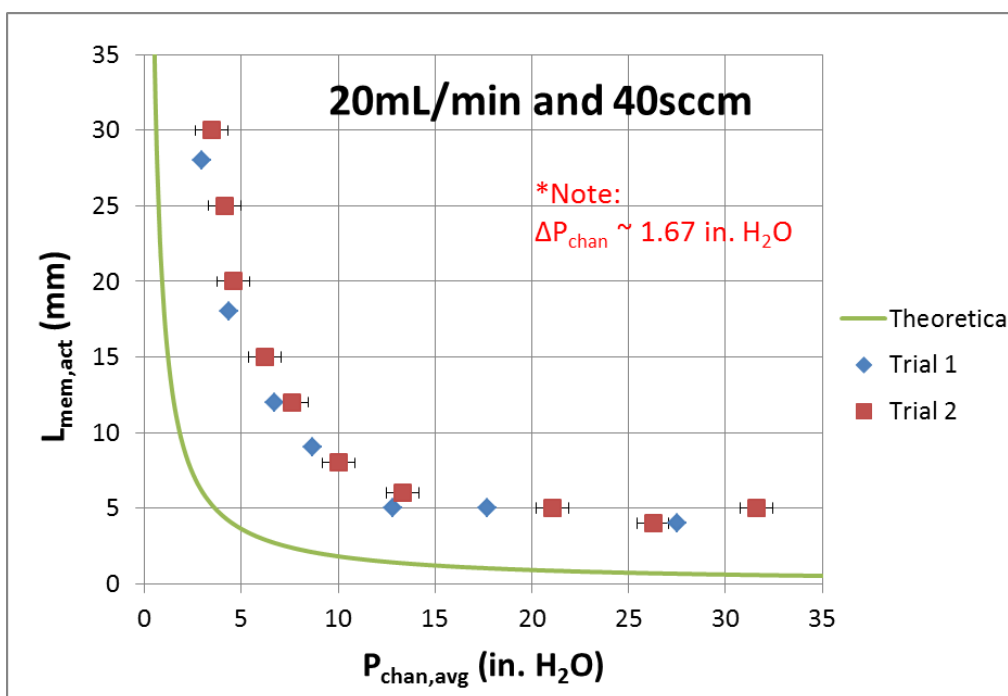


Figure 5-8: Active membrane length data for 20mL/min and 40sccm gas flow.

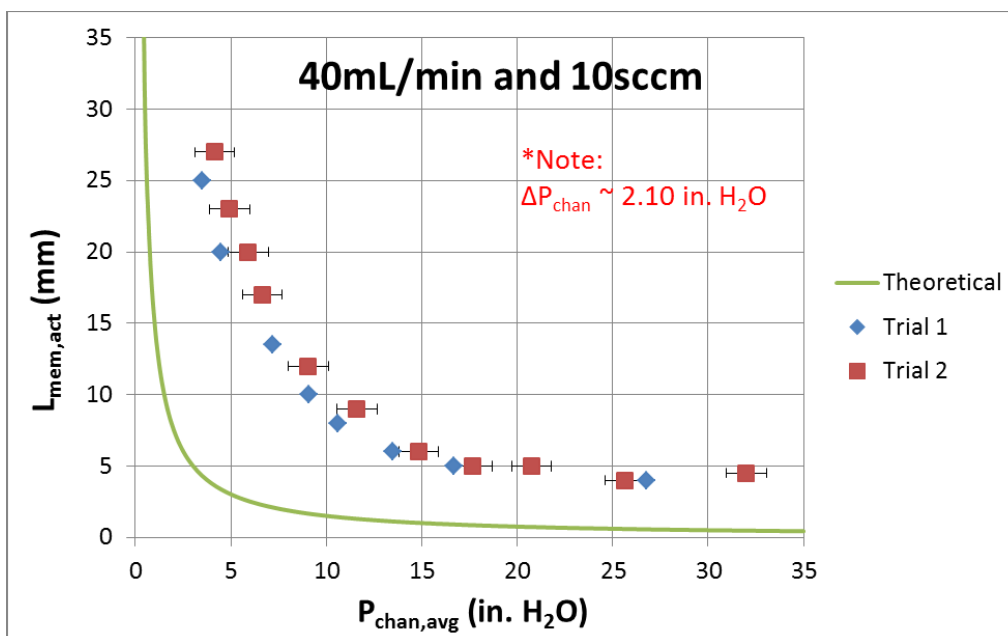


Figure 5-9: Active membrane length for 40mL/min liquid flow and 10sccm gas flow.

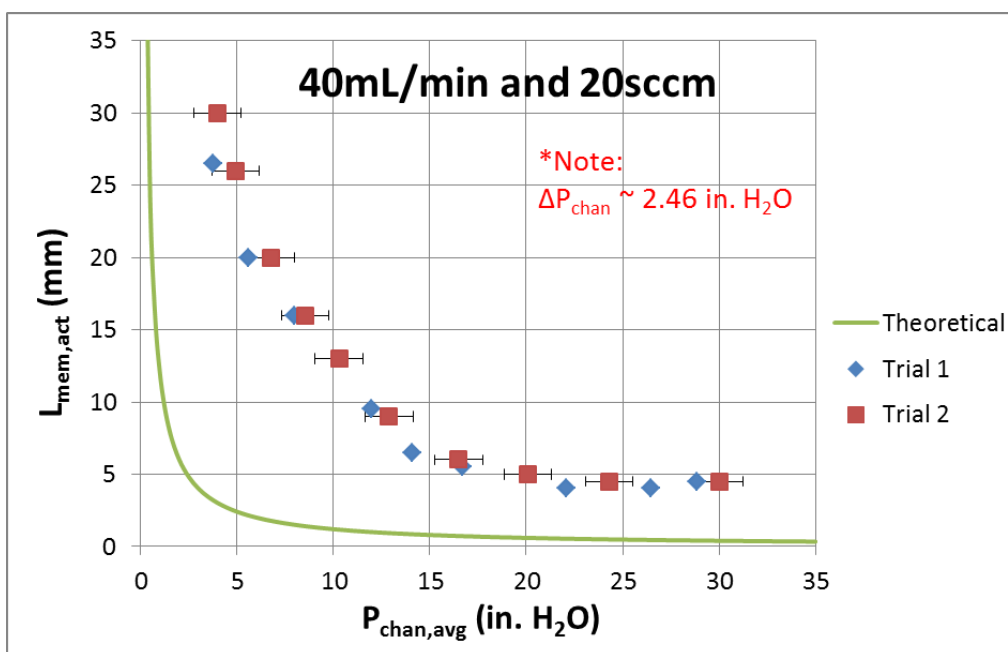


Figure 5-10: Active membrane length for 40mL/min liquid flow and 20sccm gas flow.

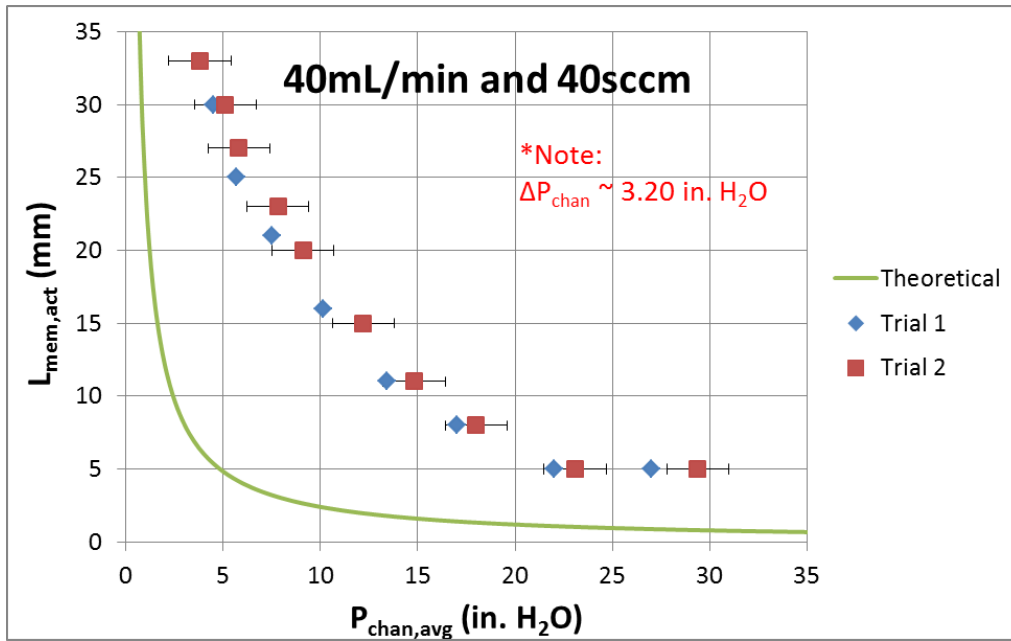


Figure 5-11: Active membrane length for 40mL/min liquid flow and 40sccm gas flow.

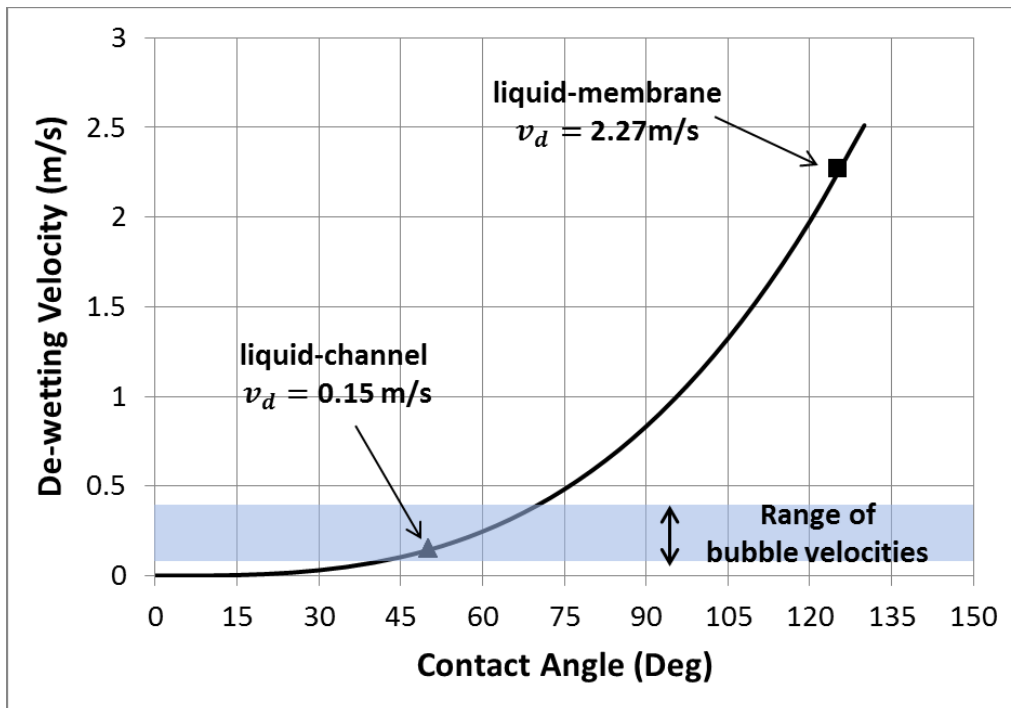


Figure 5-12: Theoretical de-wetting velocity as a function of the static contact angle for water at 21°C.

Constant Gas Flow Curves

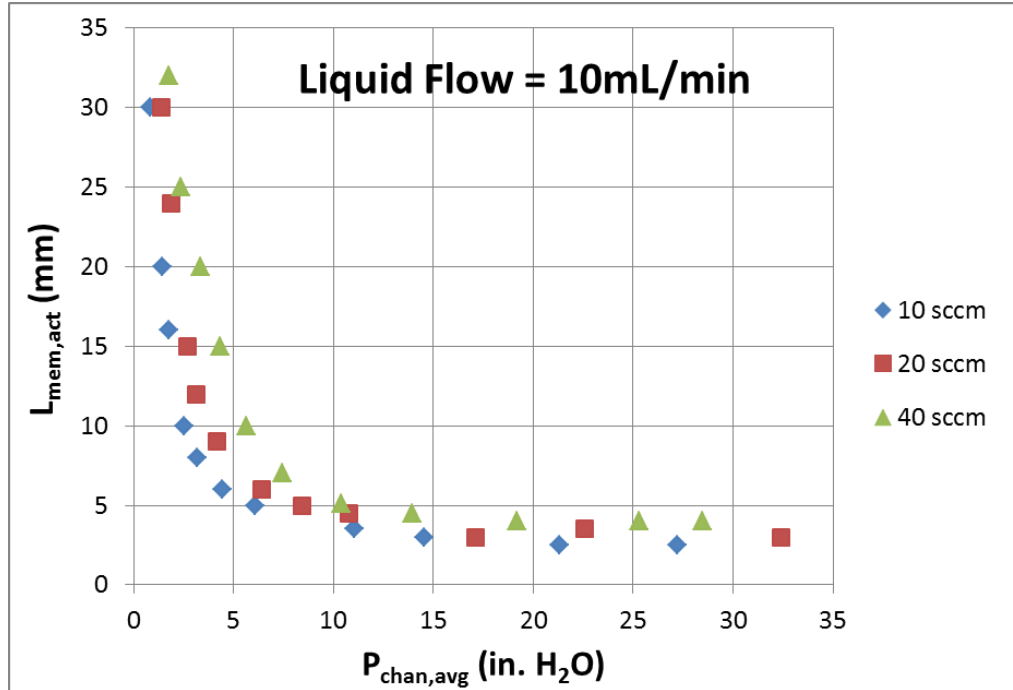


Figure 5-13: Constant gas flow curves for 10mL/min liquid flow experiment.

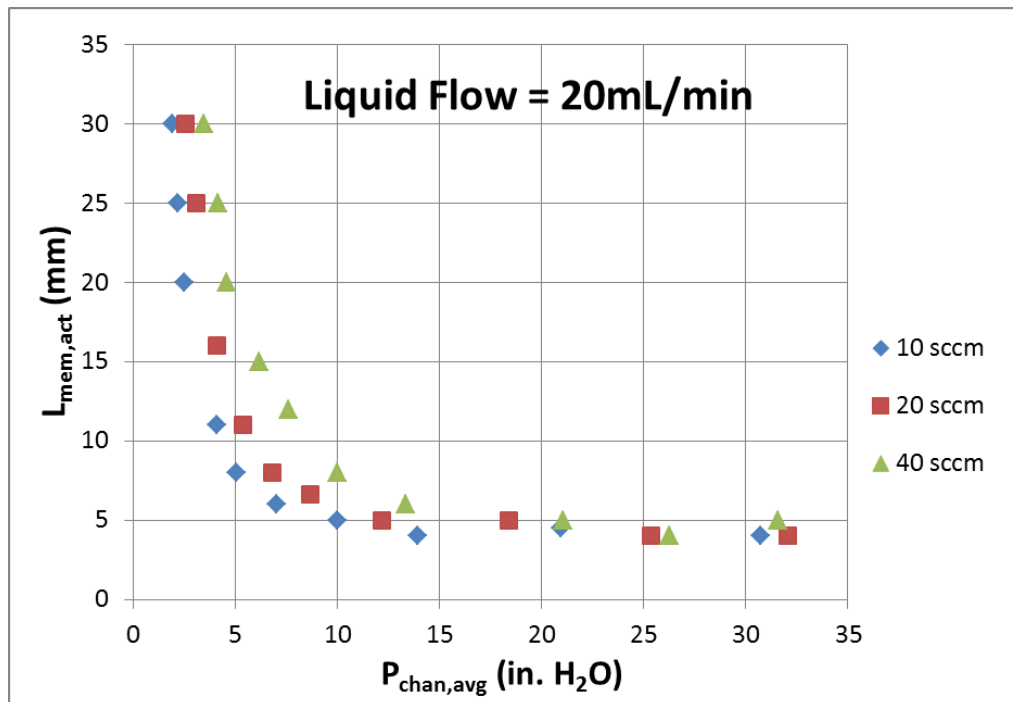


Figure 5-14: Constant gas flow curves for 20mL/min liquid flow experiment.

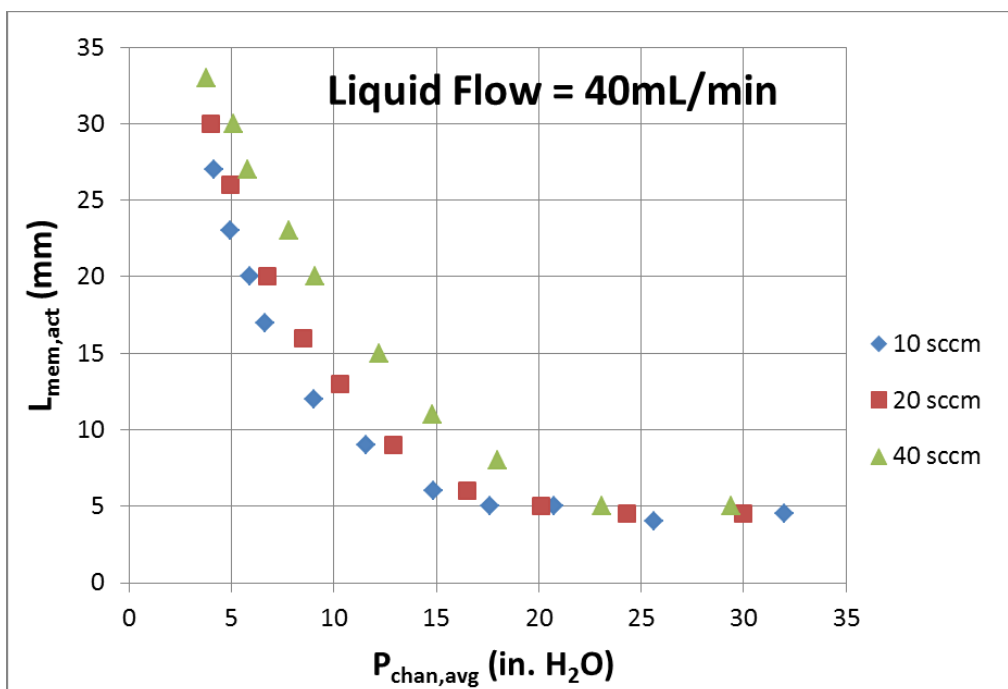


Figure 5-15: Constant gas flow curves for 40mL/min liquid flow experiment.

Constant Liquid Flow Curves

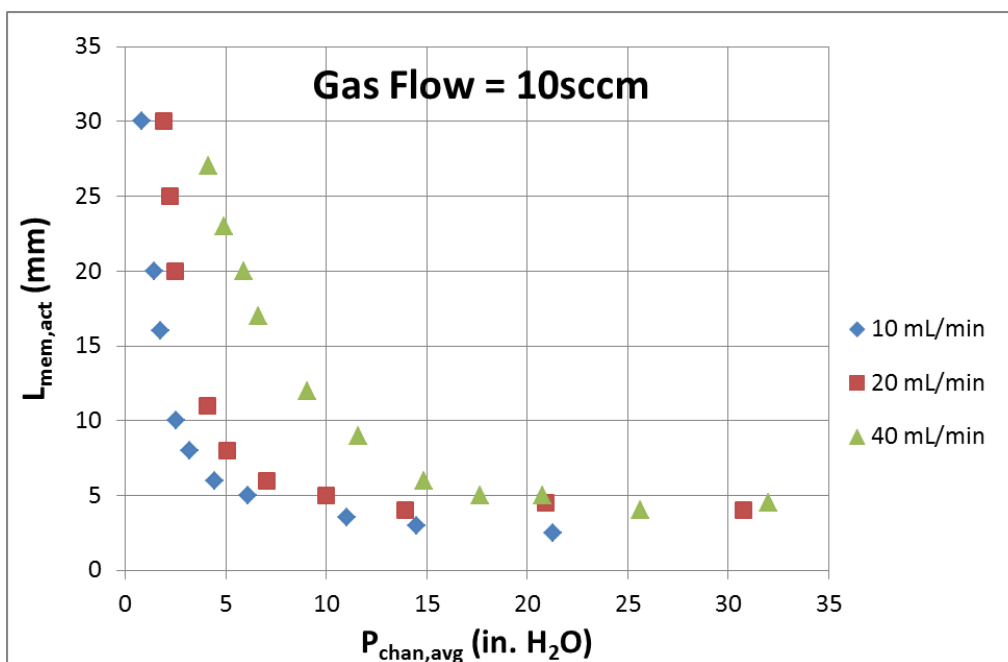


Figure 5-16: Constant liquid flow curves for 10sccm gas flow experiment.

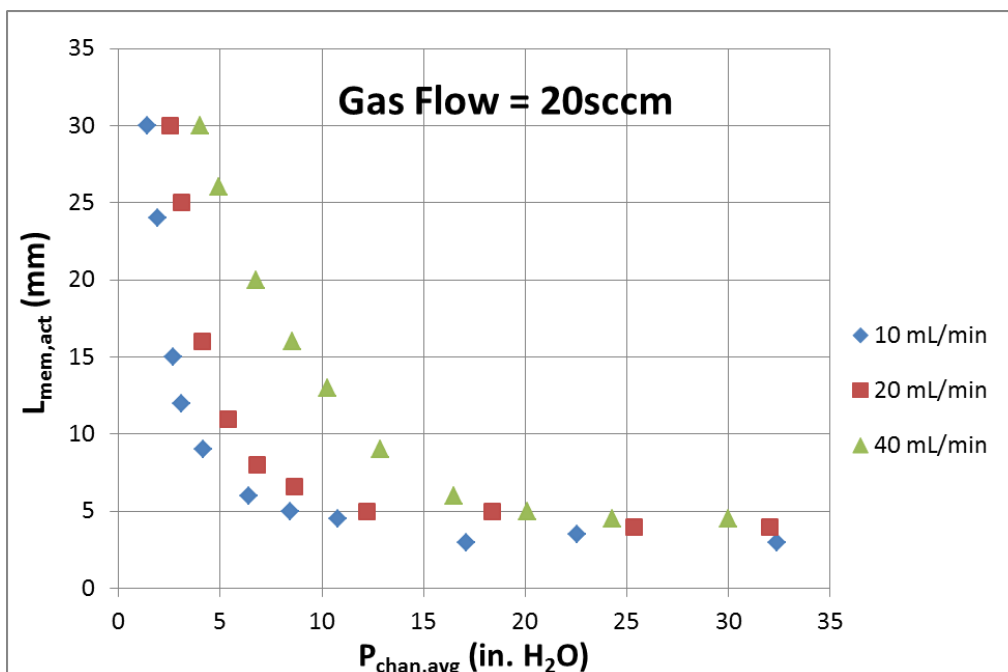


Figure 5-17: Constant liquid flow curves for 20sccm gas flow experiment.

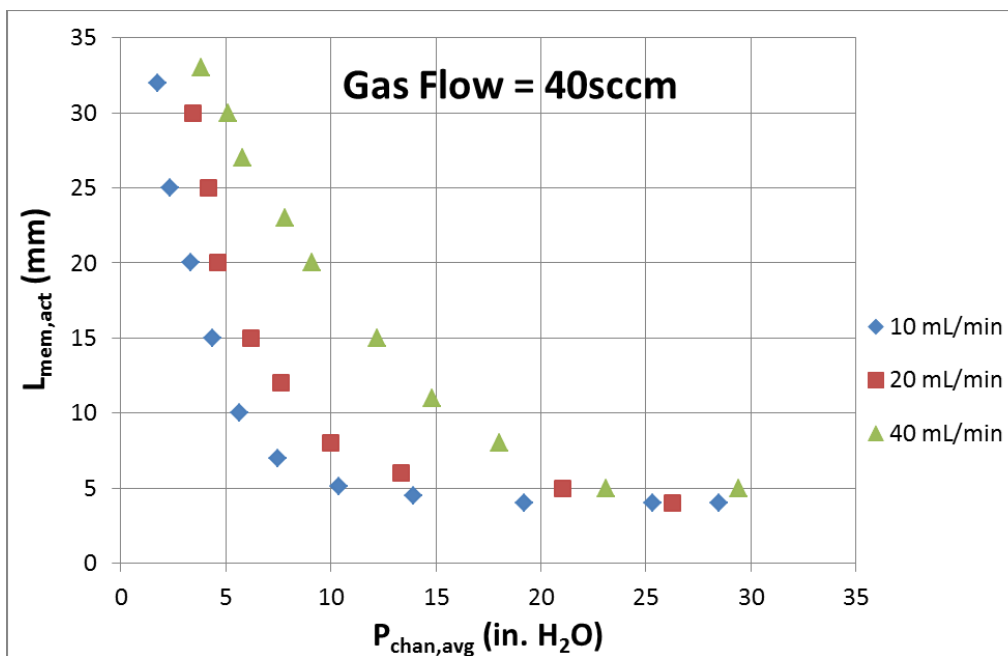


Figure 5-18: Constant liquid flow curves for 40sccm gas flow experiment.

Two-Phase Flow Patterns

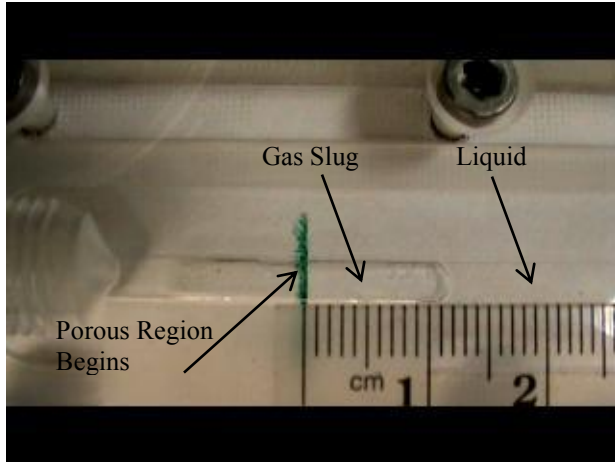


Figure 5-19: Liquid = 10mL/min, Gas = 40sccm

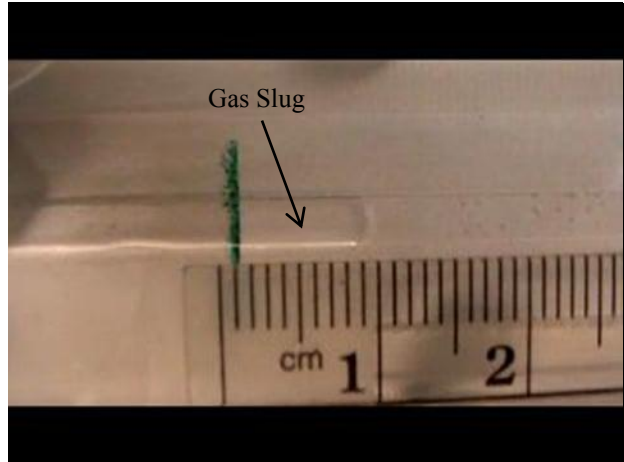


Figure 5-20: Liquid = 20mL/min, Gas = 40sccm

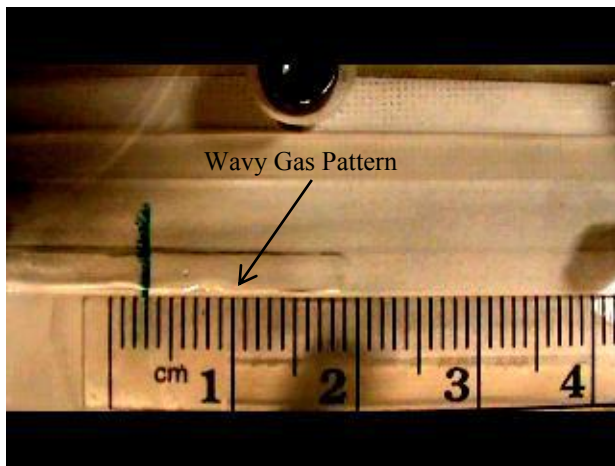


Figure 5-21: Liquid = 40mL/min, Gas = 10sccm

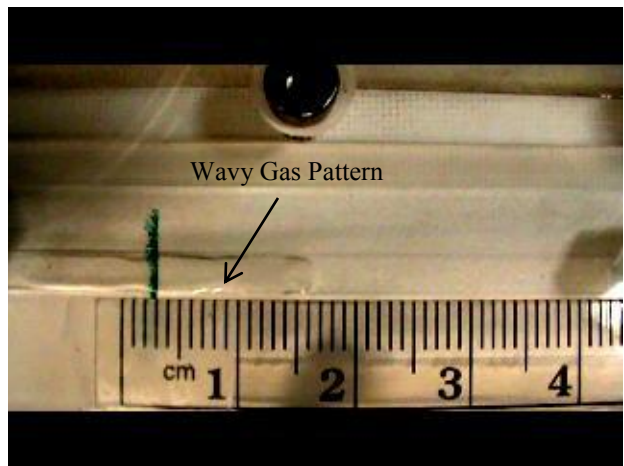


Figure 5-22: Liquid = 40mL/min, Gas = 20sccm

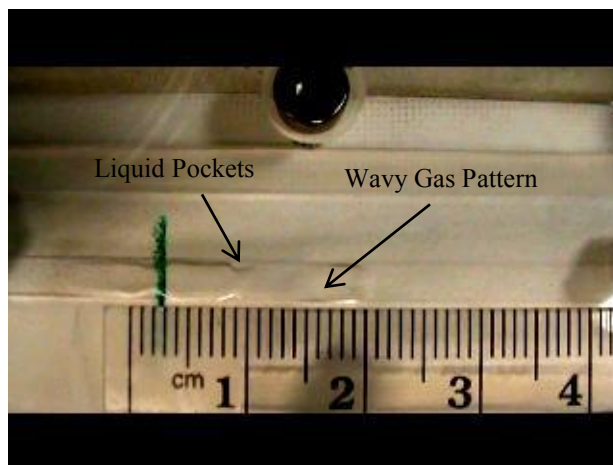


Figure 5-23: Liquid = 40mL/min, Gas = 40sccm

CHAPTER 6 CONCLUSION

As stated in chapter 1, the objective of this work was to demonstrate how the amount of porous membrane required to separate 100% of the gas bubbles from a two-phase (gas-liquid) flow could be significantly reduced simply by increasing the system pressure (i.e. applying back pressure). In order to quantify this behavior, it was first necessary to characterize the EPTFE membrane. This was done by conducting a series of membrane permeability experiments using the experimental setup illustrated in Figure 4-2. Once an overall membrane permeability coefficient was determined, it was incorporated into a mathematical model (Eq. 3-11), which predicted the ideal active membrane length as a function of the gas viscosity μ , membrane permeability K_d and thickness δ_t , channel height h_{chan} , superficial bubble velocity of the incoming two-phase flow \vec{v}_1 , and the average channel pressure $P_{chan,avg}$. The liquid entry pressure (LEP) of the membrane was estimated to be ~15 psig by using the experimental setup shown in Figure 4-3. This property was then used as a boundary condition to ensure that the gas venting process was not disrupted by any liquid-filled pores. Finally, a series of active membrane experiments were performed for a variety of two-phase flow conditions and the results were discussed and compared to the theoretical model.

Overall, it was determined that for the range of flows considered, the application of back pressure reduced the amount of active membrane by 85-93% of its original length. However, for a given channel pressure, the values of the active membrane length were consistently greater than the corresponding theoretical values, which resulted in a constant offset between the two

curves for each experiment. Since the effects of diffusion and channel pressure drop were negligible and the data curves were similar in nature to the theoretical model, the offset was attributed to a partial interference of the liquid phase, which was believed to have been caused by an insufficient de-wetting velocity of the liquid-channel system.

Furthermore, the rate at which the active membrane could be reduced with respect to the channel pressure (i.e. the curve slope) was determined to be highly dependent on the specific combination of gas and liquid flow used in each experiment. For instance, the slope of all constant gas flow curves decreased with increasing gas flow in a manner similar to that predicted by the theoretical model. This behavior was also true when increasing the liquid flow from 10 and 20mL/min; however, this was not the case when the liquid flow was increased from 20 to 40mL/min. The inadequate de-wetting velocity, responsible for the constant offset mentioned earlier, was believed to have been particularly unfavorable for gas venting in the 40mL/min liquid flow experiments, such that the two-phase flow structure was forced to transition from the wedging/slug flow regime to a less desirable wavy/semi-annular regime.

From the flow structure images in Figure 5-21 through Figure 5-23, it was deduced that the gas bubbles were forced to travel further downstream before being completely vented, since they were clearly not in direct contact with the surrounding surfaces 100% of the time. These findings suggested that if a design application requires high liquid flow rates, then the channel area should be increased until the liquid velocity is small enough to maintain a wedging/slug-like flow structure. One should also consider implementing a channel material that possess a liquid contact angle greater than 90° , to ensure that the de-wetting velocity for all wetted surfaces does not have the potential to be exceeded by the superficial bubble velocity, and thus hinder the gas venting process.

Though the method of GLS miniaturization discussed in this work was rather simplistic, the results clearly demonstrated that by applying back pressure, the amount of porous membrane required to separate a two-phase fluid was significantly reduced. This method would be particularly useful for GLS applications where the device is operating near atmospheric conditions; since the exit port area could easily be sized to induce an appropriate amount of channel pressure. The methods of determining the membrane permeability and LEP were also found to achieve accurate and consistent results for implementation into a mathematical model. Determination of the theoretical active membrane length using Eq. 3-11, while initially intended for the separation of a single bubble, proved to give adequate results for a known bulk two-phase flow. However, if more accurate results are required, the model should include a pressure drop term to account for the changing membrane wall velocity along the channel.

Future work in this field should focus on the following:

- Developing a more robust theoretical model that accounts for the buoyancy forces of the gas bubbles at different orientations.
- Ex-situ de-wetting velocity experiments should be carried out to more accurately characterize the effect of having a liquid in simultaneous contact with surfaces of drastically different hydrophobic properties.
- The effect of temperature and surfactants should also be investigated to determine conditions where the application of back pressure provides no useful benefit for GLS miniaturization.

Lastly, since the available literature does not provide enough quantitative data for a direct comparison with the current work, the theoretical model should be verified for different combinations of gas and liquid flow to ensure that the model maintains reasonable accuracy for all possible slug-flow conditions. This information would be useful for sizing future GLS designs because the need for efficient, small-sized gas-liquid separators is likely to increase as the demand for smaller portable devices, such as DMFCs and heat exchangers, increase.

REFERENCES

- [1] Y.J. Chuang, C.C. Chieng, C. Pan, S.J. Luo, F.G. Tseng, J Micromech Microengineering, 17 (2007) 915.
- [2] D.D. Meng, J. Kim, C.J. Kim, J Micromech Microengineering, 16 (2006) 419.
- [3] X. Zhu, Microsystem Technologies, 15 (2009) 1459-1465.
- [4] D.D. Meng, C.J. Kim, J.Power Sources, 194 (2009) 445-450.
- [5] M. Kraus, U. Krewer, Separation and Purification Technology, 81 (2011) 347-356.
- [6] D.D. Meng, T. Cubaud, Chih-Ming Ho, Chang-Jin Kim, Microelectromechanical Systems, Journal of, 16 (2007) 1403-1410.
- [7] J. Xu, R. Vaillant, D. Attinger, Microfluidics and nanofluidics, 9 (2010) 765-772.
- [8] M.P. David, J.E. Steinbrenner, J. Miler, K.E. Goodson, Int.J.Multiphase Flow, 37 (2011) 1135-1146.
- [9] C. Fang, M. David, A. Rogacs, K. Goodson, Frontiers in Heat and Mass Transfer, 1 (2010) 1-11.
- [10] T. Cubaud, C.M. Ho, Phys.Fluids, 16 (2004) 4575.
- [11] J. Xu, P. Cheng, T. Zhao, Int.J.Multiphase Flow, 25 (1999) 411-432.
- [12] T. Wilmarth, M. Ishii, Int.J.Heat Mass Transfer, 37 (1994) 1749-1758.
- [13] Y. Taitel, A. Dukler, AIChE J., 22 (1976) 47-55.
- [14] J. Wijmans, R. Baker, J.Membr.Sci., 107 (1995) 1-21.
- [15] E.A. Mason, A. Malinauskas, Gas transport in porous media: the dusty-gas model, Elsevier Amsterdam; 1983.
- [16] E. Mason, A. Malinauskas, R. Evans III, J.Chem.Phys., 46 (1967) 3199.
- [17] K.W. Lawson, D.R. Lloyd, J.Membr.Sci., 124 (1997) 1-25.

- [18] L. Martinez, F. Florido-Diaz, A. Hernandez, P. Pradanos, J.Membr.Sci., 203 (2002) 15-27.
- [19] P. Shao, R. Huang, X. Feng, W. Anderson, AIChE J., 50 (2004) 557-565.
- [20] H. Yasuda, J. Tsai, J Appl Polym Sci, 18 (1974) 805-819.
- [21] C.M. Gijjt, T. Reith, A.È.B. de Haan, Desalination, 132 (2000) 255-261.
- [22] W. Schneider, Acta Mech., 47 (1983) 15-25.
- [23] P. Uchytíl, R. Petrickovic, S. Thomas, A. Seidel-Morgenstern, Separation and purification technology, 33 (2003) 273-281.
- [24] M.C. Garcia'a-Payo, M.A. Izquierdo-Gil, C. Fernández-Pineda, J.Colloid Interface Sci., 230 (2000) 420-431.
- [25] P.G. De Gennes, F. Brochard-Wyart, D. Quéré, Capillarity and wetting phenomena: drops, bubbles, pearls, waves, Springer Verlag; 2004.

BIOGRAPHICAL SKETCH

Taylor Patrick Maxwell was born He graduated from Booker T. Washington High School in 2005. While enrolled at the University of North Florida (Jacksonville, Florida), Taylor was a member of the Society of Mechanical Engineers (ASME), earned his bachelor's degree in 2009, and majored in mechanical engineering with a 3.65 GPA. In January 2010, he began pursuing his master's degree in mechanical engineering (with a concentration in thermal/fluid sciences) at the University of North Florida. His graduate research involved component analysis and system integration for a portable 20 Watt direct methanol fuel cell power supply. Taylor finished his master's degree in July 2012 with a 3.5 GPA.